Chapter 3

GPS-Based Velocity and Strain Rate Field along the Himalayan Arc

" *Space in general gave us GPS – that's not specifically NASA, but it's investments in space.*"

by Neil deGrasse Tyson

This chapter presents a brief overview of the regional GPS network, data collection and

the Himalayan arc.

Content

Parts of this chapter have been published in the following refereed publications:

1. **Y. Sharma**, S. Pasari, K.E. Ching, O. Dikshit, T. Kato, J.N. Malik, C.P. Chang, and J.Y. Yen, "Spatial distribution of earthquake potential along the Himalayan arc", *Tectonophysics*, vol. 791, pp. 228556, 2020. (SCI)
(https://doi.org/10.1016/j.tecto.2020.228556)

2. **Y. Sharma**, S. Pasari, and Neha, "Indian plate motion revealed by GPS observations: preliminary results", In: R. Kulshrestha, C. Shekhar, M. Jain, and S.R. Chakravarthy (Eds.) *Mathematical Modeling and Computation of Real-Time Problems: An Interdisciplinary Approach*, CRC Press, 2021. (Scopus)
(https://doi.org/10.1201/9781003055037-15)

3.1 Introduction

Surveying has been an essential element in the development of the human environment since the beginning of the recorded history. It is the science of measuring the relative position of points on the ground to understand kinematic details above, on, or beneath the Earth's surface. It is required in the planning and execution of nearly every form of construction and measuring natural or human-induced hazards. Snell Van Royan was one of the first Dutch surveyors who measured baselines and interior angles of a triangular mesh to determine the position of points at a long distance from a given origin [101]. Further, the triangulation technique was widely adopted by surveyors to determine positions and motions over the larger continents. However, this technique has major drawbacks in the mountain areas, where the baselines get extended by some amount [101]. As an advancement of the triangulation method, many other techniques have evolved such as the optical global triangulation and the electromagnetic global trilateration. The optical global triangulation derives position on the ground by correlating the paths between Earth, stars, and satellites. The electromagnetic global trilateration was initially used to measure the position of aircraft by connecting the continents using electronic High-Range Navigation (HIRAN) system. By implementing the Doppler shift, it was used to determine the instantaneous precise position on the ground [101].

In the 1960s, the US military developed a satellite-based program, known as Navy Navigation Satellite System (NNSS), to determine precise coordinates of army ships in the sea and to track enemy missiles [101]. Further, this program was partially available for civilian uses such as navigation and surveying purposes. However, this program has several shortcomings, such as the huge gaps between two satellites and low navigation accuracy [101]. To overcome such shortcomings, a new satellite system, Navigation System with Timing and Ranging (NAVSTAR) Global Positioning System (GPS), was launched by the US military to aid precise positioning, timing, and velocity on the ground as well as in the space under almost all weather conditions [92, 101].

3.2 GPS overview

The Global Positioning System (GPS) is a space-based navigation system stabilized by the US Department of Defense (DoD) in the early 1970s. It comprises three main segments: the space segment, control segment, and the user segment (Fig. 3.1). Space

segment consists of 31 satellites placed in six different orbital planes at an inclination of 55° and elevation of 20,200 km above the Earth's surface (Fig. 3.1) [101]. Each satellite transmits data at two different L-band carrier frequencies of L1 = 1575.42 MHz and L2 = 1227.69 MHz. The L-band carries the navigation message which consists of the ephemeris information, predicted GPS satellite orbits, clock corrections, ionospheric noise, and satellite health status [81, 292]. The control segment contains one Master Control Station (MCS), one alternative MCS, 16 monitoring stations, and 11 control and command antennas. The main jobs of this segment are tracing the satellite orbit, determining clock corrections, and formulating navigation data. These informations are then modulated on the S-band frequency and uploaded back into GPS satellites (Fig. 3.1). The user segment includes the GPS receivers that use the received information from the satellites to calculate its position and time (Fig. 3.1) [101].

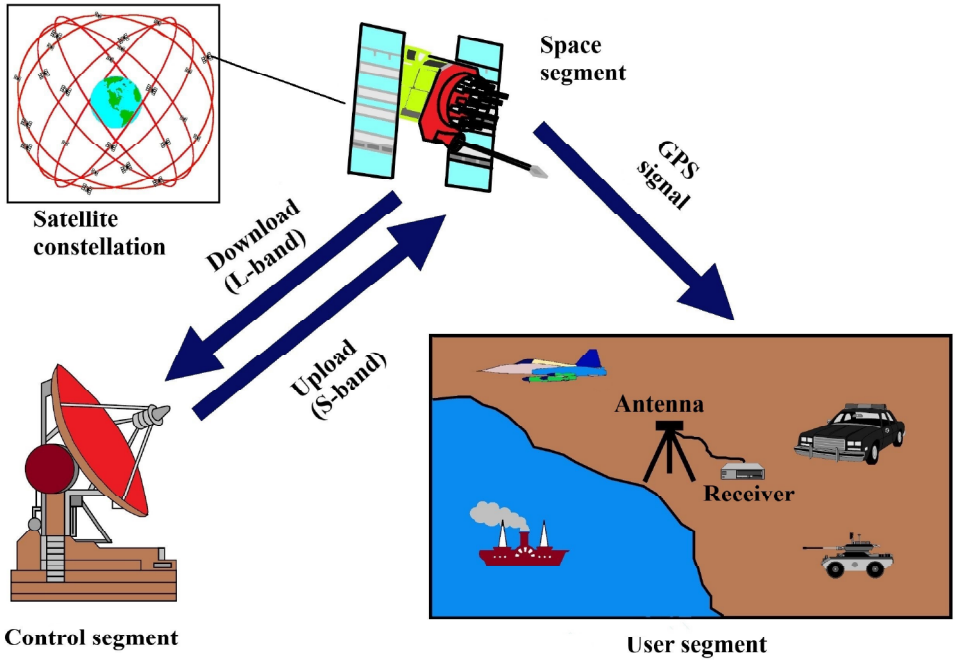

Fig. 3.1: GPS segments and satellite constellation (Hofmann et al. (2012) [101]).

The clock reading at the satellite antenna is compared with a clock reading at the receiver antenna. This comparison provides the pseudorange (distance) from receiver

antenna to the tracking satellite and the time of traveling of signal (between satellite-receiver combination) [101, 292]. The pseudorange can be formulated as below.

$$R = \rho_r^s + c\Delta\delta + d_{ion} + d_{trop} + d_{tide} + \varepsilon_p \tag{3.1}$$

Here,

$$\rho_r^s = \sqrt{((X^s(t) - X_r)^2 + (Y^s(t) - Y_r)^2 + (Z^s(t) - Z_r)^2)} \tag{3.2}$$

is the geometric range between satellite and receiver antenna; $X^s(t)$, $Y^s(t)$, $Z^s(t)$ are the components of the geocentric position vector of the satellite at epoch t; X_r, Y_r, Z_r are three coordinates of the observing receiver; c is the speed of light; $\Delta\delta$ is the offset between the receiver clock and the satellite clock; d_{ion}, d_{trop}, and d_{tide} are the ionospheric delays, tropospheric delays, and tidal loading effects, respectively; and ε_p represents the effect of multipath and receiver noise [81, 92, 101, 292] .

On the other hand, the carrier phase is a measure of the phase difference between the received carrier and the signal generated by the GPS receiver. Positioning accuracy from the carrier phase (ϕ) is about ten times better than the accuracy of code pseudoranges [81, 92, 101, 292]. The carrier phase equation can be represented as follows.

$$\lambda\phi = \rho_r^s + c\Delta\delta + \lambda N + d_{ion} + d_{trop} + d_{tide} + \varepsilon_p \tag{3.3}$$

Here, N is the ambiguity related to the receiver and satellite (number of fractional phase) and λ is the carrier wavelength [81, 92, 101, 292]. There are many sources of error that could affect the accuracy of GPS observations. These are ionospheric and tropospheric delays, satellite orbital errors, ocean tide loading effect, receiver and satellite clock biases, multipath noises, and others. To reduce these errors in the estimation of GPS coordinates and relative velocity, a linear combination approach is often used [81, 92, 101, 292]. Particularly, receiver and satellite clock biases can be significantly reduced using the double-difference method [101]. To understand the double-difference method, let us assume two receivers a, b and two satellites j, k. Two carrier phase observation equations according to Equation (3.3) can be written as:

$$\lambda\phi_a^j = \rho_a^j + c\Delta\delta_a + \lambda N_a^j + d_{a\ ino}^j + d_{a\ trop}^j + d_{a\ tide}^j + \varepsilon_{a\ p}^j \tag{3.4}$$

$$\lambda\phi_b^j = \rho_b^j + c\Delta\delta_b + \lambda N_{ab}^j + d_{b\ ino}^j + d_{b\ trop}^j + d_{b\ tide}^j + \varepsilon_{b\ p}^j \tag{3.5}$$

First, the single difference is performed for satellite j and receivers a and b by subtracting Equation (3.4) from Equation (3.5).

$$\lambda\phi_{ab}^{j} = \rho_{ab}^{j} + c\Delta\delta_{ab} + \lambda N_{ab}^{j} + d_{ab\ ino}^{j} + d_{ab\ trop}^{j} + d_{ab\ tide}^{j} + \varepsilon_{ab\ p}^{j} \tag{3.6}$$

Similarly, the single difference for satellite k and receivers a and b is obtained as:

$$\lambda\phi_{ab}^{k} = \rho_{ab}^{k} + c\Delta\delta_{ab} + \lambda N_{ab}^{k} + d_{ab\ ino}^{k} + d_{ab\ trop}^{k} + d_{ab\ tide}^{k} + \varepsilon_{ab\ p}^{k} \tag{3.7}$$

To obtain a double-difference equation, the single-difference equations are subtracted (Equation (3.7) from Equation (3.6))

$$\phi_{ab}^{jk} = \frac{1}{\lambda}\rho_{ab}^{jk} + N_{ab}^{jk} + \frac{1}{\lambda}(d_{ab\ ino}^{jk} + d_{ab\ trop}^{jk} + d_{ab\ tide}^{jk} + \varepsilon_{ab\ p}^{jk}) \tag{3.8}$$

The advantage of the double difference is that the receiver clock biases are completely removed and the ionospheric and tropospheric effects have been reduced to a great extent [81, 92, 101, 292]. These corrected GPS observations are now used to calculate the position and relative velocity of the receiver.

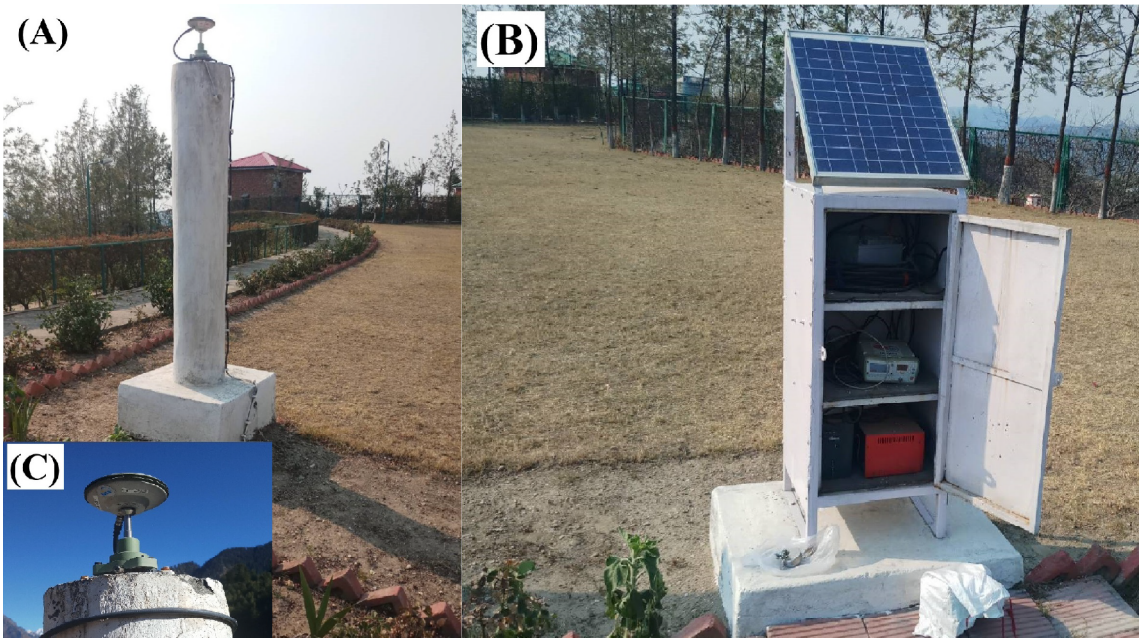

Fig. 3.2: A typical setup of a continuous GPS station at Jaypee University, Samirpur (Himachal Pradesh). (A) RCC pillar; (B) enclosure of GPS receiver, UPS power back up, internal batteries, and solar panels; (C) GPS antenna on RCC pillar.

3.3 GPS network and data collection

In order to understand the topography and near-fault crustal deformation, a GPS network was established in 2013-14 along the northwest Himalaya (Fig. 3.3). The regional network comprising three arc-normal (T1, T2, and T3) transects and one arc-parallel (T4) transect covers the megathrust system of the Himalaya.

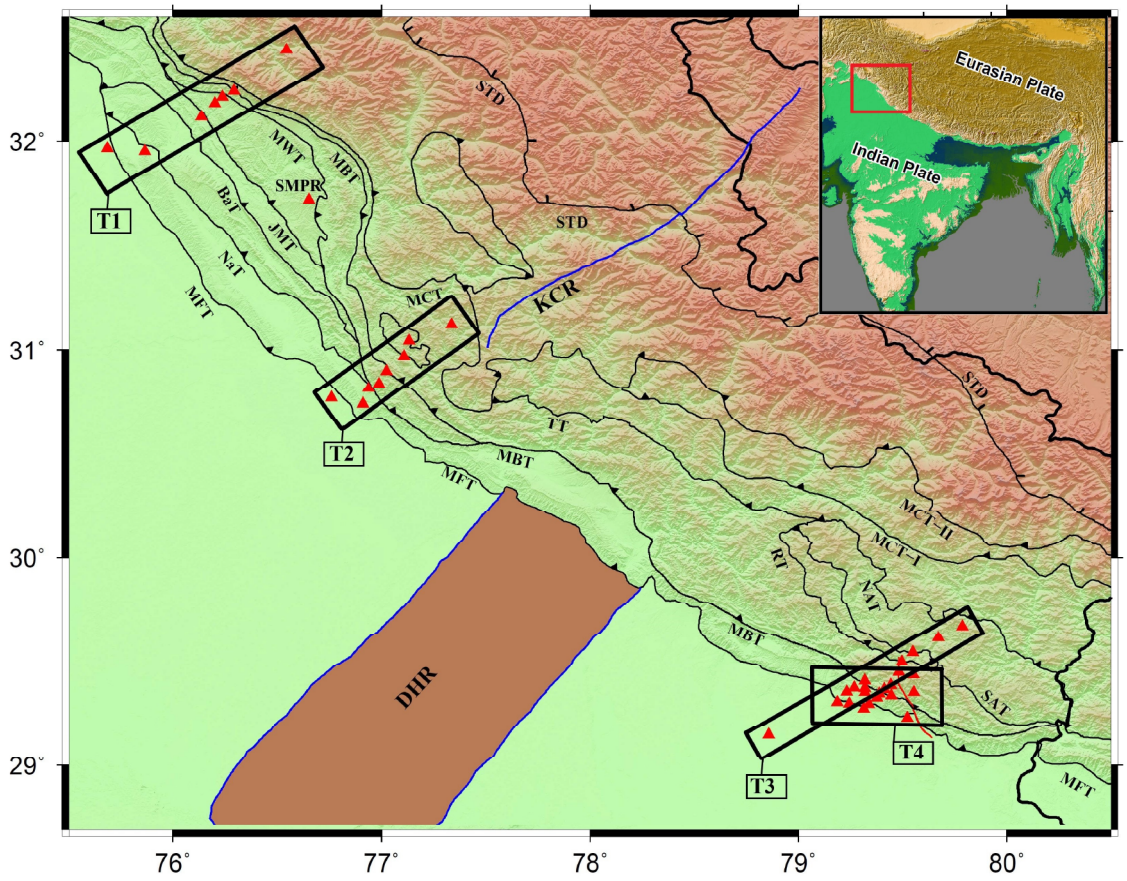

Fig. 3.3: GPS network along the northwest Himalaya. Abbreviations are as follows: BaT, Barsar Thrust; DHR, Delhi-Haridwar Ridge; JMT, Jawalamukhi Thrust; KCR, Kaurik Chango Rift; MBT, Main Boundary Thrust; MCT, Main Central Thrust; MFT, Main Frontal Thrust; MWT, Medilicott- Wadia Thrust; NaT, Nalagarh Thrust; NAT, North Almora Thrust; RT, Ramgarh Thrust; SAT, South Almora Thrust; STD, South Tibetan Detachment; TT, Tons Thrust.

Each of these north-south arc-normal transects contains two permanent GPS stations at its ends. In addition, six to eight campaign-surveyed GPS stations were established for the densification of the network (Fig. 3.3). Two other permanent GPS stations were

also set up at Indian Institute of Technology Kanpur and at Jaypee University, Samirpur (Himachal Pradesh). Apart from this, the arc-parallel (T4) transect containing 13 campaign-mode GPS stations was established in the Nainital region in the beginning of 2014 (Fig. 3.3). Each permanent station is constructed on a concrete pillar on top of which the GPS antenna is mounted (Fig. 3.2). The GPS receiver, connecting cables, solar panels, an Uninterrupted Power Supply (UPS) for the power back up, and internal batteries for an emergency are placed to complete the site establishment (Fig. 3.14). All campaign sites are chosen on the Reinforced Cement Concrete (RCC) government or private building rooftops with a clear sky visibility. In this study, Leica GR25 GNSS receiver and Leica AS10 high-performing geodetic quality antenna have been used for permanent GPS stations. For campaign-mode stations, Leica Viva GS15 geodetic quality antenna and Leica Viva GS15 GNSS receiver have been utilized. The GS15 receiver and GS15 antenna are connected by Bluetooth. Further, the location co-ordinates, measurement mode, and observation times of each station in each transect is summarized in Table 3.1 to Table 3.4.

Table 3.1: Details of GPS stations in transect T1

GPS Station	Longitude (°E)	Latitude (°N)	Observation mode	Time period of observation
MUKE	75.6849	31.9682	Continuous	2013 onwards
BBMB	75.8651	31.9528	Campaign	2013–2015
MNAI	76.1356	32.1181	Campaign	2013–2015
KOTH	76.2003	32.1834	Campaign	2013–2015
THAR	76.2370	32.2135	Campaign	2013–2015
SATO	76.2922	32.2432	Campaign	2013–2015
BRMR	76.5436	32.4397	Continuous	2013 onwards

The transect T1 extends from Mukerian (Punjab) to Bharmour (Himachal Pradesh) (Fig. 3.4). The southernmost station in this transect is located at Mukerian (75.6849° E, 31.9682° N) in the quaternary foreland of IGP. This is a permanent GPS station, installed on a RCC pillar in the open lawn of a private school, Sri Guru Gobind Singh Senior Secondary Public School at Kamlooh, Mukerian. The northern most site of this transect is located at Bharmour (76.5436° E, 32.4397° N). This continuous station is setup on a concrete pillar in an open boundary of a government guest house lawn of Himachal

Pradesh Irrigation Department at Bharmour, situated on the sedimentary rocks of Lesser Himalaya. In between these two permanent stations, five campaign-mode stations were also setup at an average distance of 8−10 km (Fig. 3.4 and Table 3.1).

From north to south, the campaign sites are SATO (76.2922° E, 32.2432° N), THAR (76.2370° E, 32.2135° N), KOTH (76.2003° E, 32.1834° N), MNAI (76.1356° E, 32.1181° N), and BBMB (75.8651° E, 31.9528° N) (Fig. 3.4 and Table 3.1). It may be noted that the Himalayan megathrusts pass through this transect, such as MFT between MUKE−BBMB, and MBT and MCT between SATO−BRMR (Fig. 3.4). Two branching faults of the MBT, namely the JMT and the MWT also pass through between MNAI−KOTH and THAR−SATO, respectively (Fig. 3.4).

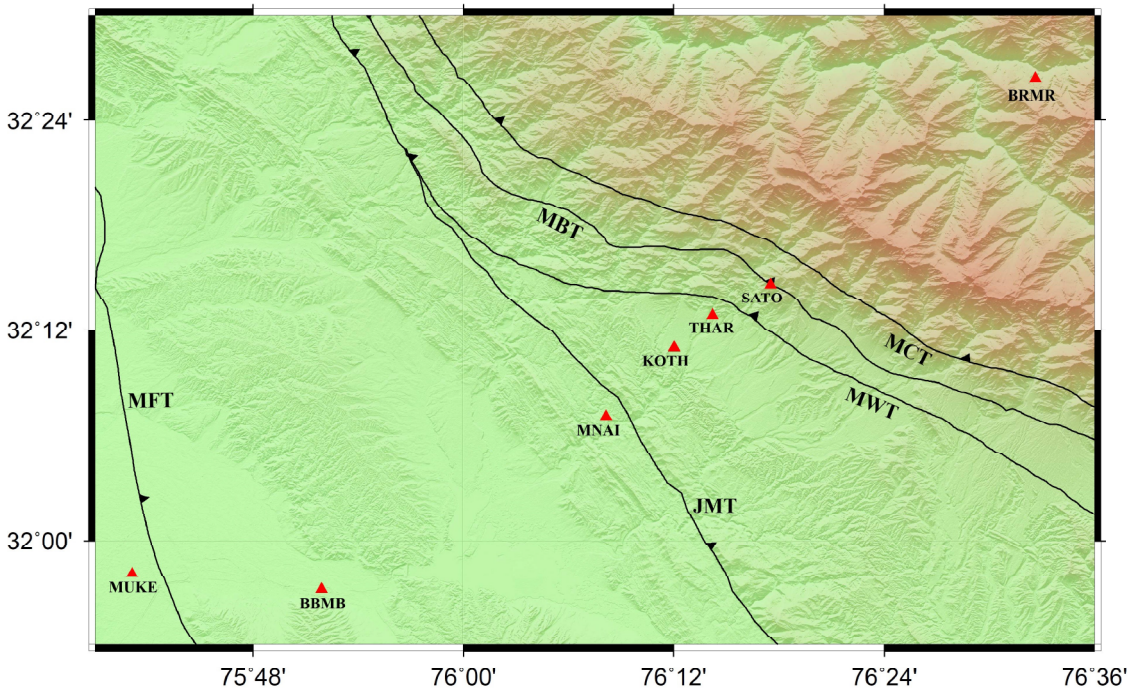

Fig. 3.4: GPS stations along transect T1. Abbreviations are as follows: JMT, Jawalamukhi Thrust; MBT, Main Boundary Thrust; MCT, Main Central Thrust; MFT, Main Frontal Thrust; MWT, Medilicott- Wadia Thrust.

The transect T2 extends from Chandigarh to Theog (Himachal Pradesh) (Fig. 3.5). The two permanent stations at the rear end of this transect were installed on the rooftop of the main building of the Geology Department of Punjab University (CHD1: 76.7609° E, 30.7674° N) along the IGP and in an open lawn of Jawahar Navodaya Vidyalaya (JNV),

Theog, Shimla (THEO: 77.3359° E, 31.1231° N) in the Lower Himalayan segment (Fig. 3.5). Six campaign mode stations were also setup in between these two continuous sites.

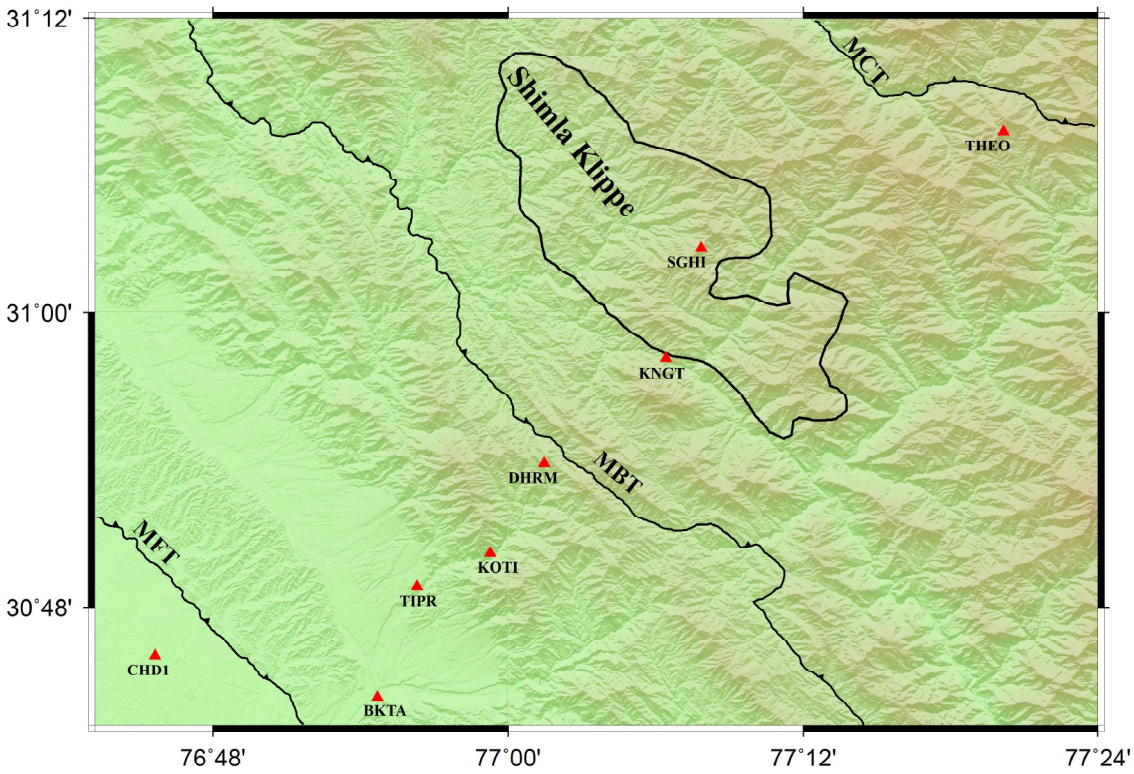

Fig. 3.5: GPS stations along transect T2. Abbreviations are as follows: MBT, Main Boundary Thrust; MCT, Main Central Thrust; MFT, Main Frontal Thrust.

From north to south, these campaign stations are SGHI (77.1309° E, 31.0440° N), KNGT (77.1071° E, 30.9692° N), DHRM (77.0244° E, 30.8976° N), KOTI (76.9879° E, 30.8368° N), TIPR (76.9385° E, 30.8139° N), and BKTA (76.9115° E, 30.7394° N) (Fig. 3.5 Table 3.2). Two major geological fault lines, namely the MFT (between CHD1−BKTA) and the MBT (between DHRM−KNGT) also route through this transect (Fig. 3.5). Apart from this, a major geological formation of the Lower Himalaya, the Shimla Klippe, also falls in the northern side of this transect (Fig. 3.5).

Table 3.2: Details of GPS stations in transect T2

GPS Station	Longitude (°E)	Latitude (°N)	Observation mode	Time period of observation
CHD1	76.7609	30.7674	Continuous	2013 onwards
BKTA	76.9115	30.7394	Campaign	2013–2015
TIPR	76.9385	30.8139	Campaign	2013–2015
KOTI	76.9879	30.8368	Campaign	2013–2015
DHRM	77.0244	30.8976	Campaign	2013–2015
KNGT	77.1071	30.9692	Campaign	2013–2015
SGHI	77.1309	31.0440	Campaign	2013–2015
THEO	77.3359	31.1231	Continuous	2013 onwards

The transect T3 comprises 10 GPS stations along the Kumaun Himalaya. Two permanent stations were installed at the rear ends of the transect. These stations are DHLC (79.7870° E, 29.6700° N), located at a private property in Dhaulachhina along the Lower Himalaya and THKD (78.8569° E, 29.1486° N), located in an open lawn of the JNVN school at Thankurdwara along the IGP (Fig. 3.6).

Table 3.3: Details of GPS stations in transect T3

GPS Station	Longitude (°E)	Latitude (°N)	Observation mode	Time period of observation
THKD	78.8569	29.1486	Continuous	2013 onwards
NYGN	79.3143	29.2743	Campaign	2013–2015
GTGH	79.3768	29.3284	Campaign	2013–2015
NATL	79.4425	29.3879	Campaign	2013–2015
RAGT	79.4809	29.4500	Campaign	2013–2015
CHRA	79.4966	29.5004	Campaign	2013–2015
JNVN	79.5488	29.5465	Campaign	2013–2015
ALMR	79.6708	29.6152	Campaign	2013–2015
DHLC	79.7870	29.6700	Continuous	2013 onwards

Other eight campaign-mode sites, from north to south, are located at ALMR (79.6708° E, 29.6152° N), JNVN (79.5488° E, 29.546° N), CHRA (79.4966° E, 29.5004° N), RAGT (79.4809° E, 29.4500° N), NATL (79.4425° E, 29.3879° N), GTGH (79.3768° E,

29.3284° N) , and NYGN (79.3143° E, 29.2743° N) (Fig. 3.6 and Table 3.3). Two major faults, namely the MFT (NYGN−GTGH) and the MBT (GTGH−MNGL) pass through this transect (Fig. 3.6). Two other branching faults, namely the SAT (near JNVN) and the RT (near CHRA) along with a transverse strike slip fault, the G-KF (prolongated from RT to further IGP crossing through the MBT and the MFT), also lie in this transect (Fig. 3.6). In addition, a geological formation, the Almora Klippe, falls in the northern part (from JNVN to further north) of this transect (Fig. 3.6).

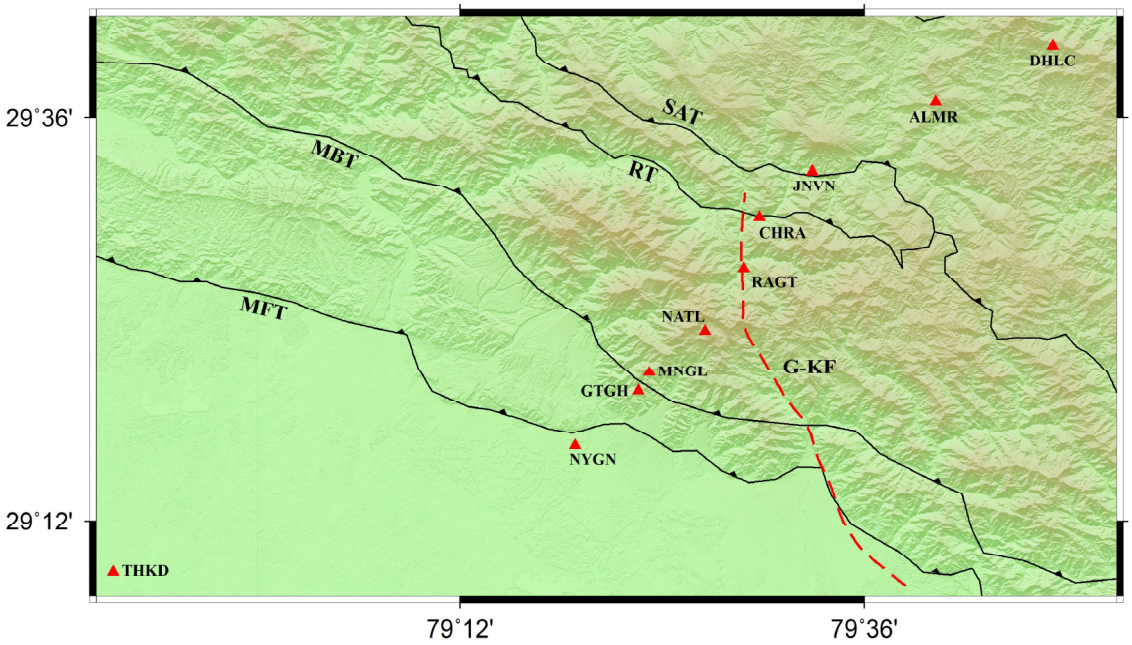

Fig. 3.6: GPS stations along transect T3. Abbreviations are as follows: G-KF, Garampani-Kathgodam Fault; MBT, Main Boundary Thrust; MFT, Main Frontal Thrust; RT, Ramgarh Thrust; SAT, South Almora Thrust.

Table 3.4: Details of GPS stations in transect T4

GPS Station	Longitude (°E)	Latitude (°N)	Observation mode	Time period of observation
I001	79.4110	29.3683	Campaign	2014–2017
I002	79.3183	29.4082	Campaign	2014–2017
I006	79.3187	29.3525	Campaign	2014–2017
I007	79.3192	29.3739	Campaign	2014–2017
I009	79.2684	29.3753	Campaign	2014–2017

I010	79.2319	29.3571	Campaign	2014–2017
I011	79.1871	29.3048	Campaign	2014–2017
I013	79.2429	29.2988	Campaign	2014–2017
I015	79.3368	29.2952	Campaign	2014–2017
I016	79.4464	29.3359	Campaign	2014–2017
I017	79.5231	29.2308	Campaign	2014–2017
I018	79.5539	29.3529	Campaign	2014–2017
I019	79.5519	29.4369	Campaign	2014–2017

The last transect, T4, in the Lower Kumaun Himalaya contains 13 campaign mode GPS stations (Fig. 3.7). These stations are I001 (79.4110° E, 29.3683° N), I002 (79.3183° E, 29.4082° N), I006 (79.3187° E, 29.3525° N), I007 (79.3192° E, 29.3739° N), I009 (79.2684° E, 29.3753° N), I010 (79.2319° E 29.3571° N), I011 (79.1871° E, 29.3048° N), I013 (79.2429° E, 29.2988° N), I015 (79.3368° E, 29.2952° N), I016 (79.4464° E, 29.3359° N), I017 (79.5231° E, 29.2308° N), I018 (79.5539° E, 29.3529° N), and I019 (79.5519° E, 29.4369° N) (Table 3.4).

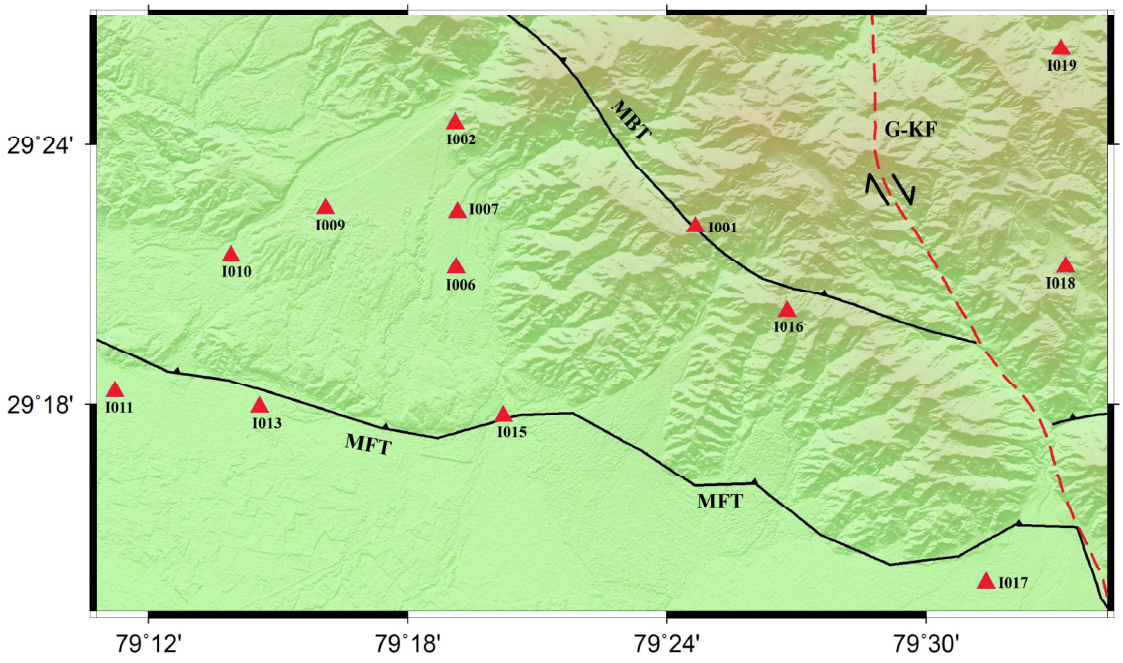

Fig. 3.7: GPS stations along transect T4. Abbreviations are as follows: G-KF, Garampani-Kathgodam Fault; MBT, Main Boundary Thrust; MFT, Main Frontal Thrust.

Unlike previous three arc-normal transects (T1, T2, and T3) that focus on the along strike fault kinematics of the Himalayan megathrust system, the purpose of this arc-parallel transect (T4) is to study the crustal deformation along the Lower Kumaun Himalaya, with an emphasis on the deformation pattern controlled by an across-strike fault, the G-KF (Fig. 3.7). This transect also cuts through two megathrusts, namely the MFT and the MBT (Fig. 3.7).

3.4 GPS data processing

Since 2013, continuous raw data are being collected throughout the year at 1s and 30s sampling interval. The purpose of 1s data is to study coseismic deformation during an earthquake. Apart from this, campaign stations are occupied twice or thrice in a year at a 1s sampling interval. Each campaign session is setup for ∼24-hour observation on a 15° elevation angle with all available satellites. All raw GPS data are then examined using the Translation, Editing, and Quality Check (TEQC) software for quality checking, such as flagging outliers and data gaps. [76]. Once the GPS data are refined and examined, the raw data are converted into Receiver Independent Exchange (RINEX) format using the TEQC software for further analysis. The RINEX files are then used for data processing. For high precision research work in geodesy, some standard scientific GPS post-processing software (GAMIT-GLOBK, BERNESE, and GIPSY) are mostly utilized. In the present study, the GAMIT-GLOBK suite post-processing software is used to analyze the accrued GPS data. This software, available in the LINUX environment, was developed by the Massachusetts Institute of Technology (MIT) for the estimation of three-dimensional relative positions of the ground station. The GAMIT uses GPS broadcast carrier phase and pseudorange observables (stored in RINEX file) known as GPS readings, satellite ephemeris (stored in navigation file), and satellite orbit data (stored in orbit file). Through the least-squares estimation, it generates values of positions and other parameters such as orbits, Earth orientation, ambiguities, and atmospheric delays [99, 150]. With this setup, the position of the receiver antenna is obtainable from Equation (3.2). The linearized form of the equation allows us to implement the least-squares algorithm. The simplified and linear form of Equation (3.2) is given below in terms of the observation equation:

$$d = Ax + v \tag{3.9}$$

where,

d $[n \times 1]$: vector of observations,

A $[n \times u]$: design matrix,

x $[u \times 1]$: vector of unknowns (parameter),

v $[n \times 1]$: noise or residual vector.

For further computation, let us define some additional parameters:

σ_0^2: a priori variance,

Σ : covariance matrix,

$Q_d = \frac{1}{\sigma_0^2}\Sigma$: the cofactor matrix of observations, and

$P = Q_d^{-1}$: the weight matrix.

The least-squares adjustment provides a unique solution of Equation (3.9) subject to the condition $v^T Pv$ = minimum.

This adjustment principle provides the following normal equation:

$$A^T PAx = A^T Pd \tag{3.10}$$

The solution of Equation (3.10) is

$$x = (A^T PA)^{-1} A^T Pd \ , \tag{3.11}$$

which can be simplified to

$$x = G^{-1} g \ , \tag{3.12}$$

where, $G = A^T PA$ and $g = A^T Pd$.

The cofactor matrix Q_x follows from $x = G^{-1} A^T Pd$ by the covariance propagation law as:

$$Q_x = (G^{-1} A^T P) Q_d (G^{-1} A^T P)^T \tag{3.13}$$

By substituting $Q_d = P^{-1}$, the above equation further reduces to

$$Q_x = G^{-1} = (A^T PA)^{-1} \tag{3.14}$$

The daily solutions from GAMIT provide location coordinates for each GPS station along with Earth orientation and satellite orbit corrections. Further, the estimated loosely constrained daily solutions are utilized to estimate station position and plate motion using the GLOBK [99].

Processing of the GPS data in the GAMIT-GLOBK is often performed in three stages: (i) all data are processed using GAMIT to obtain loosely constrained solutions of coordinates of a particular station together with IGS (International GNSS Service) fiducial stations, (ii) the time series of position coordinates of every station is then examined for outliers using GG-MATLAB (GAMIT-GLOBK MATLAB) tool, and finally (iii) the refined time-series data are utilized for the station velocity estimation in GLOBK [99]. For the data processing, the below step-by-step process is followed:

Step 1: First, install the GAMIT-GLOBK software in a LINUX environment. Also, check a few important files:

process.defaults (edit to specify computation environment, source for internal and external data and orbit files, start time sampling interval, and instructions for archiving the results)

sestbl. (edit the *AUTCLN* postfit command to suit processing strategy)

sites.defaults (edit to specify sites to ftp from RINEX data archives, to search for RINEX files on the local system, and to exclude from automatic *station.info* updating)

station.info (edit to include all continuous stations as well as all IGS stations)

and ***lfile., leap.sec, luntab., nutabl.*** (these files need to be up to dated).

Step 2: Prepare four subdirectories in an experimental directory: brdc (contains navigation (.n) files), igs (contains sp3 or orbit files (.sp3) of satellite for all the

used IGS stations), rinex (contains all the RINEX files (.o) of observations of regional as well as IGS stations), and tables (tables folder of GAMIT).

To download the observation, navigation, and orbit-sp3 files for the chosen IGS stations, the following commands are used:

(i) **RINEX files**: *sh_get_rinex -archive <archive> -yr <year> -doy <day of year> -ndays <number of days> -sites <IGS sites>*

<archive> here the observation files of the IGS stations are stored (e.g., SOPAC, CDDIS, MIT, and others)

<year> year of observation

<day of year> day of observation in the corresponding year

<number of days> number of consecutive days of data to retrieve

<IGS sites> List of IGS stations to be retrieved from archive (e.g., here 16 IGS stations are used: CHUM, COCO, DGAR, DRAG, GUAO, HYDE, IISC, KIT3, KRTV, LCK2, LHAZ, PLO2, SOLA, TEHN, URUM, and WUHN)

Example *sh_get_rinex -archive sopac -yr 2020 -doy 301 -ndays 5 -sites HYDE IISC*

(ii) **Navigation files**: *sh_get_nav -archive <archive> -yr <year> -doy <day of year> -ndays <number of days>*

Example *sh_get_nav -archive sopac -yr 2020 -doy 301 -ndays 5*

(iii) Orbit/SP3 files *sh_get_orbit -archive <archive> -yr <year> -doy <day of year> -ndays <number of years> -type <type of orbit file sp3/gfile> -center <IGS processing center igs/esa/sio>*

Example *sh_get_orbit -archive sopac -yr 2020 -doy 301 -ndays 5 -type gfile -center igs*

Step 3: After downloading all required files (observation, navigation, and orbit files), a global tide model FES2004 (*otlFES2004.grid*) is utilized to account for solid Earth tides and ocean loading effects. Subsequently, a series of GAMIT commands are used:

sh_gamit -d yr days/-s yr d1 d2 -expt -orbit -aprfile -yrext

-d yr days (need to use if data are processed for each specified day (e.g., 2020 301 305 306))

-s yr d1 d2 (need to use if data are processed for continuously from starting day to *n* number of days (e.g., 2020 301 310))

-expt (four character experiment name (e.g., BITS))

-orbit (type of orbit to be used (e.g., IGSF, SIOF, and others))

-aprfile (name of reference frame (e.g., itrf2008.apr)

-yrext (to specify output directory by corresponding year and day (e.g., 2020_301))

Example *sh_gamit -d 2020 301 306 -expt BITS -orbit SIOF -aprfile itrf2008.apr -yrext*

Step 4: GAMIT provides a sequence of daily station coordinates in terms of *h*-files of loosely constrained solutions. However, the existing outliers (e.g., unleveled antenna error, multipath effect, snow on antenna, and others) are hard to identify from the GAMIT output files. However, the time series plottings of the station coordinates allow us to identify outliers. In this regard, the GLRED program is often used. It generates a time series of three dimensional positions (North, East, and UP) using the following commands.

(i) Create two subdirectories (**glbf** and **gsoln**) in the main experimental directory.

(ii) Convert all the ASCII *h*-files into binary *h* files (readable to GLRED and GLOBK) using **htoglb** (*htoglb [glbf_directory] [ephemeris_file] <GAMIT h-file>*). Then copy all binary *h*-files into **glbf** directory together with SOPAC global binary *h* files from the IGS network (*sh_get_hflies*).

(iii) Create a list of binary *h*-files in the **gsoln** directory using *ls ../glbf/h*.glx >expt.gdl*. Also copy *globk_rep.cmd* and *globk_vel.cmd* files from **table** directory.

(iv) Run GLRED using

glred <crt> <prt> <log> <input_list> <globk cmd file>

Example *glred 6 globk_rep.prt globk_rep.log expt.gdl globk_rep.cmd -mb*

The last term *−mb* creates multibase (time series) files, which are further executable in *tsveiw* program of **GG-MATLAB** (GAMIT-GLOBK MATLAB) tool to remove outliers, seasonal modulations, and others, as necessary[99].

Step 5 Once all corrections and refinement of data are made, the data are filtered through GLOBK to obtain the station velocity using the following command:

globk <crt> <prt> <log> <input_list> <globk cmd file> VEL

Example *globk 6 globk_vel.prt globk_vel.log expt.gdl globk_vel.cmd VEL*

The above process generates a *globk_vel.org* file, which contains three dimensional (north, east, and up) velocity of a station. The velocity information of several stations will enable deriving a velocity field for the study region.

3.5 GPS time series and velocity field

The final estimated daily positions at each site were transformed into the International Terrestrial Reference Frame 2008 (ITRF08) for further analysis [6]. Fig. 3.8 to Fig. 3.19 represent time series plots in the north, east, and upward direction of all stations along the northwest Himalaya. The discontinuities or jumps that occur in the GPS position time series are possibly due to receiver stoppage, antenna error, multipath effect, or seasonal variation. The seasonal variation is found to be large in vertical component of displacement, whereas minor variations can be observed in the north and east components for all stations. The modulations of seasonal variation can be the combination of surface loading related to water variations, ionospheric-tropospheric pressure, and vapor loading during the winter season [63]. The seasonal effect can be decomposed into the annual and semi-annual components in terms of a linear function of sine and cosine terms:

$$y(t) = a + b \times t + c \times cos(2\pi t/T) + d \times sin(2\pi t/T) + e \times cos(4\pi t/T) + f \times sin(4\pi t/T) \tag{3.15}$$

Here, a is the intercept (constant value); b is the secular rate; c and d are the amplitude annual (12 months) periodic perturbations (sine and cosine terms); and e and f are the

amplitude semi-annual (six months) periodic disturbances (sine and cosine terms).

The amplitude of the semi-annual seasonal effect is generally smaller than the annual seasonal effects. It has been noted that continuous observations for a longer time span (>2.5 years) reduce the influence of seasonal variations in the estimation of station velocity [39]. By a visual inspection of time-series for each station in *tsveiw* program of GG-MATLAB, outliers are marked and subsequently eliminated on a case-by-case basis. Further, the Kalman filter of GLOBK is used to compute the interseismic deformation velocity for each site from daily positions, refined from a time-series analysis in the ITRF08 reference frame [99]. The station velocities in the ITRF08 reference frame show a general northeast trend of the Indian plate motion, though the localized deformation within the study region is hard to visualize. As a result, the India-fixed reference frame or the Eurasia-fixed reference frame is often preferred. In the India-fixed reference frame, the site velocities are displayed with respect to the fixed India plate, by using a rotation pole information, for example, latitude $51.698 \pm 0.271^{\circ}$N, longitude $11.853 \pm 1.790^{\circ}$N, and rotation rate 0.553276 ± 0.005520 M/yr given by Jade et al. (2017) [116]. The horizontal and vertical velocities of all GPS stations for each transect are summarized in Table 3.5 to Table 3.8 and are pictorially shown in Fig. 3.20 to Fig. 3.22.

In transect T1, horizontal velocities (ITRF08 frame) in the north direction vary between 24.99 ± 1.99 mm/yr and 35.08 ± 2.01 mm/yr, whereas in the east direction, they vary between 25.72 ± 0.79 mm/yr and 31.33 ± 1.99 mm/yr (Fig. 3.20 and Table 3.5). Similarly, in the India-fixed reference frame, all sites move with a velocity between -0.55 ± 2.01 mm/yr and 9.55 ± 1.99 mm/yr in the south direction and between 0.70 ± 1.99 mm/yr and 6.26 ± 0.79 mm/yr in the west direction (Fig. 3.21 and Table 3.5). The vertical component of velocities of this transect shows subsidence from the sites MUKE to THAR and uplift along Lesser (SATO site) to Higher Himalaya (BRMR site) with rates lying between 0.12 ± 0.44 mm/yr and 5.01 ± 7.78 mm/yr and between 2.43 ± 0.43 mm/yr and 10.82 mm/yr, respectively (Fig. 3.22 and Table 3.5).

In transect T2, surface velocities (ITRF08 frame) in the north direction vary between 32.11 ± 0.66 mm/yr and 34.85 ± 1.57 mm/yr, whereas in the east direction, they vary between 30.96 ± 0.77 mm/yr and 34.82 ± 1.47 mm/yr (Fig. 3.20 and Table 3.6). In the India-fixed reference frame, all stations move with a rate between -0.07 ± 1.57 mm/yr and 2.57 ± 0.60 mm/yr in the south direction and between -1.66 ± 1.47 mm/yr and 2.16 ± 0.77 mm/yr in the west direction (Fig. 3.21 and Table 3.6). The vertical velocity of the CHD1 site shows large subsidence with a rate of 11.61 ± 0.25 mm/yr. In the frontal Himalaya, a

continuous upliftment is evident between the sites BKTA and DHRM with the velocities ranging between 5.78±5.71 mm/yr and 17.53±9.17 mm/yr (Fig. 3.22 and Table 3.6). Moving further in the north direction, a persistence subsidence (∼10 mm/yr) is observed between the sites SGHI and THEO.

In transect T3, horizontal velocities (ITRF08 frame) in the north direction vary between 28.85±1.53 mm/yr and 36.28±1.54 mm/yr, whereas in the east direction, they vary between 28.06±1.93 mm/yr and 36.01±1.75 mm/yr (Fig. 3.20 and Table 3.7). In the India-fixed reference frame, the southernmost station (THKD) shows insignificant (0.07±0.40 mm/yr) eastward motion, however, the sites between NYGN and RAGT move (1.01±1.37 mm/yr to 6.81±1.93 mm/yr) in the west direction, except GTGH, which indicates a slightly eastward motion (1.09±1.75 mm/yr) (Fig. 3.21 and Table 3.7). Further in the north of the Nainital region, an eastward motion (0.74±1.75 mm/yr to 0.80±1.44 mm/yr) of the sites (CHRA, JNVN, and ALMR) indicates distinct deformation pattern in comparison to the stations (THKD to RAGT) situated below Nainital (Fig. 3.21 and Table 3.7). Similarly, the pattern of the vertical velocity reveals different regional tectonics in north and south of the Nainital region. In the south (THKD to NATL), a continuous subsidence (0.13±8.61 mm/yr to 11.55±5.99 mm/yr) is observed, whereas in the north (RAGT to DHLC), a persistent uplift motion (2.32±0.43 mm/yr to 11.62±5.37 mm/yr) is evident (Fig. 3.22 and Table 3.7).

In transect T4, surface velocities (ITRF08 frame) in the north direction vary between 30.18±2.53 mm/yr and 34.06±1.59 mm/yr, whereas in the east direction, they vary between 32.40±1.14 mm/yr and 37.33±1.74 mm/yr (Fig. 3.20 and Table 3.8). In the India-fixed reference frame, all stations move with a velocity between −1.28±1.59 mm/yr and 5.19±2.53 mm/yr in south direction and between −2.48±1.74 mm/yr to 3.39±1.61 mm/yr in the west direction (Fig. 3.21 and Table 3.8). In the vertical component, the sites I001, I006, I007, I007, I011, I015, I018, and I019 show subsidence with velocities ranging between 1.87±8.24 mm/yr to 16.30±6.95 mm/yr, whereas the sites I002, I010, I013, I016, and I017 revel uplift displacement with rates ranging between 1.84±7.65 mm/yr and 6.08±6.30 mm/yr (Fig. 3.22 and Table 3.8).

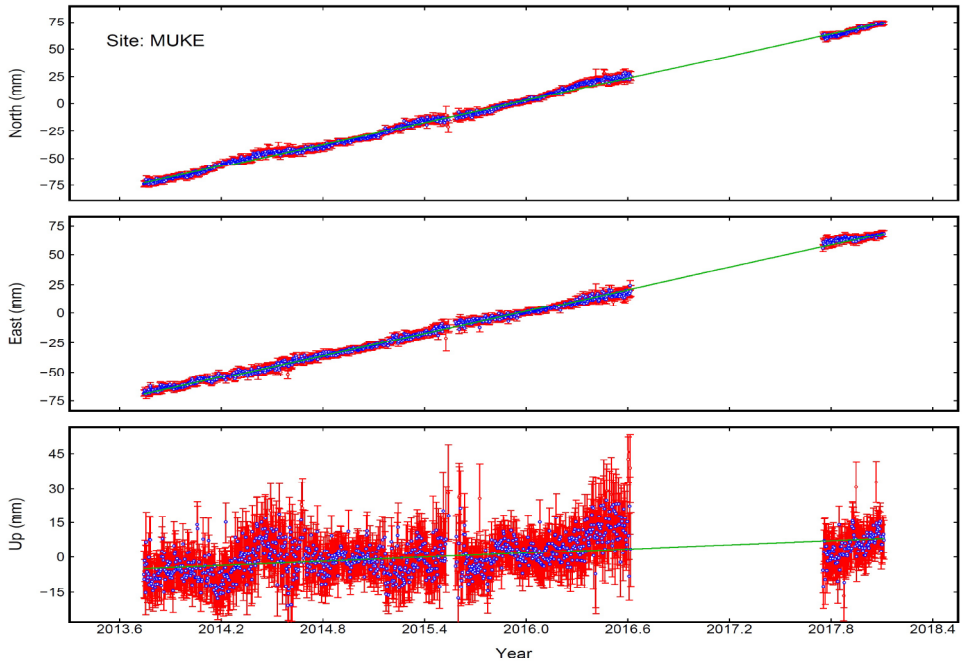

Fig. 3.8: Time series plot of MUKE station.

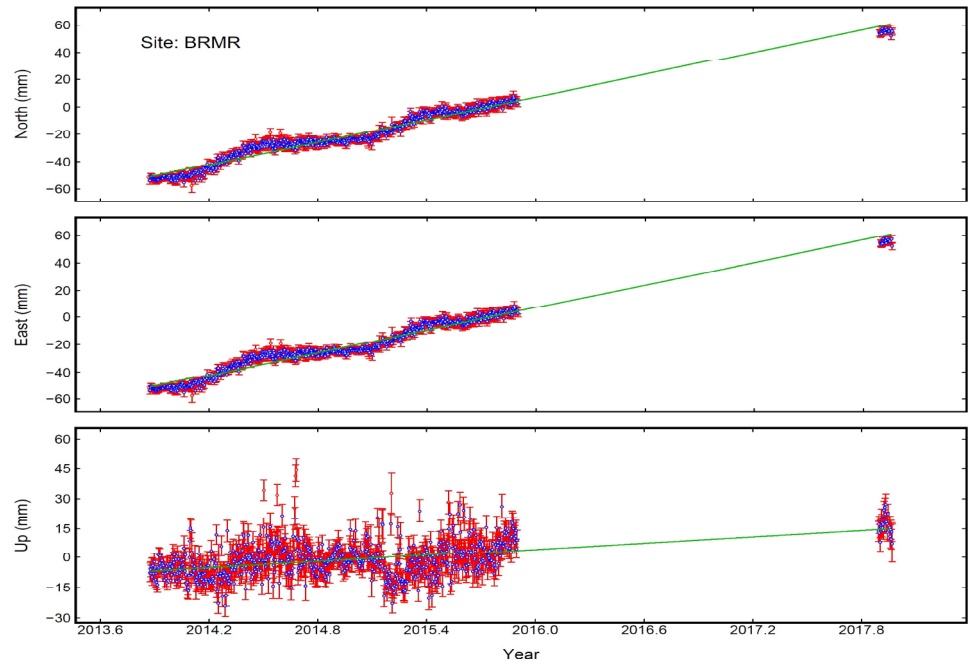

Fig. 3.9: Time series plot of BRMR station.

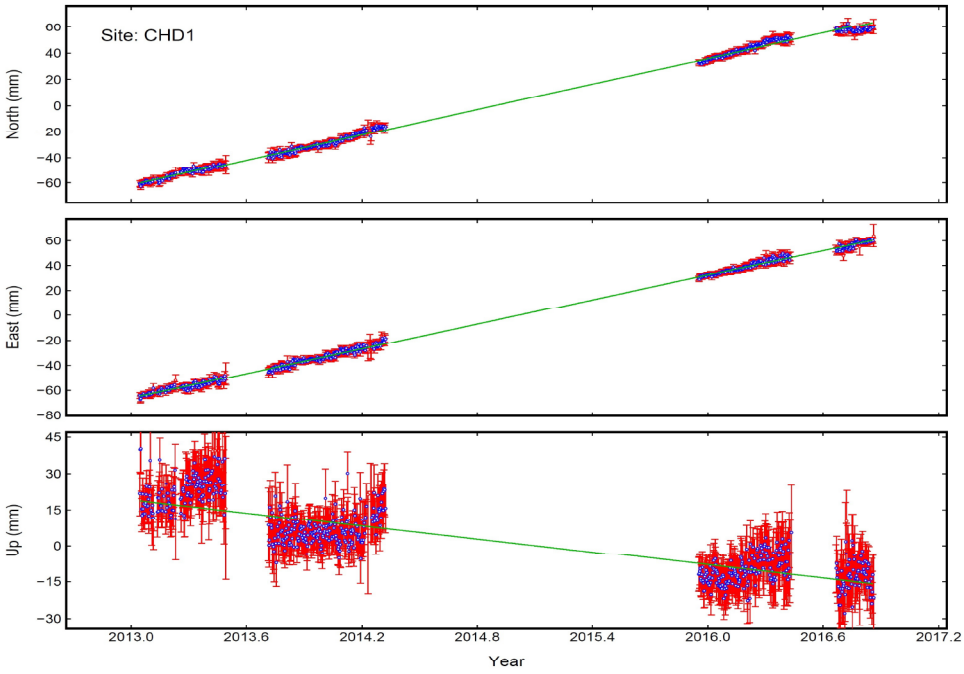

Fig. 3.10: Time series plot of CHD1 station.

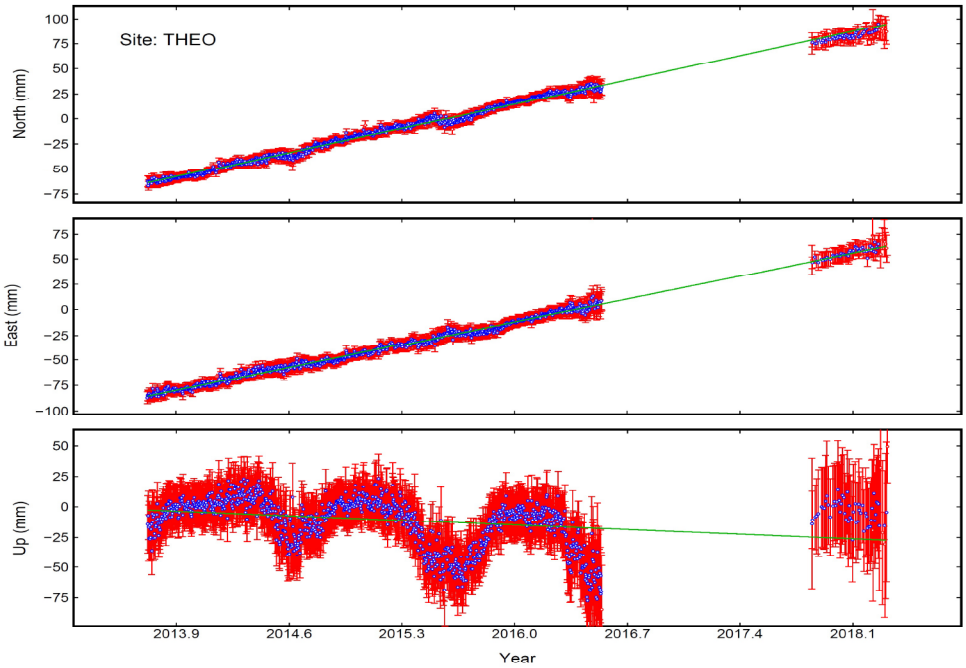

Fig. 3.11: Time series plot of THEO station.

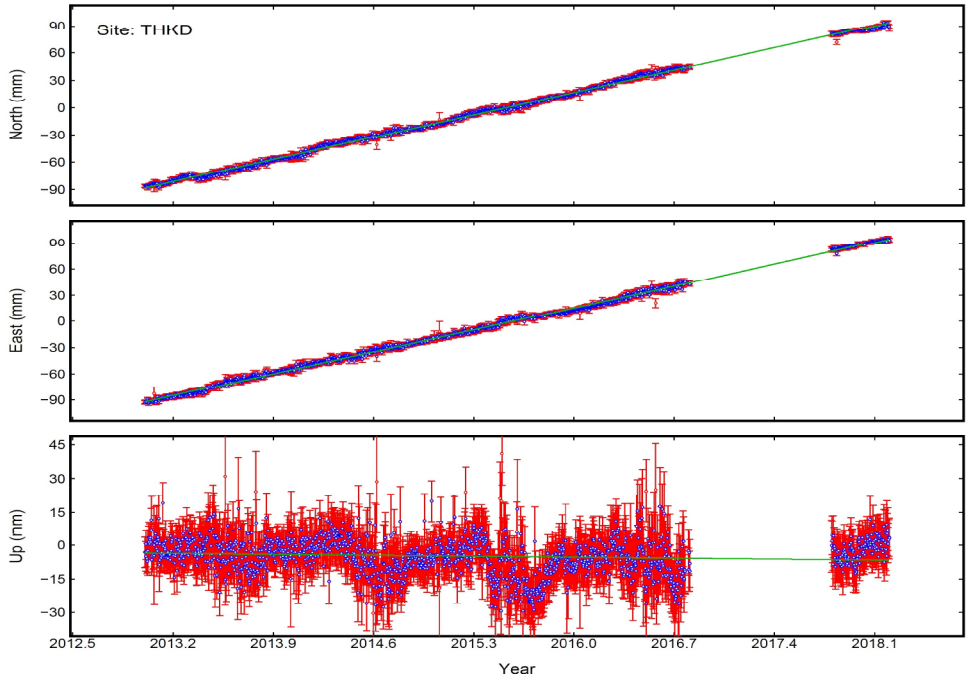

Fig. 3.12: Time series plot of THKD station.

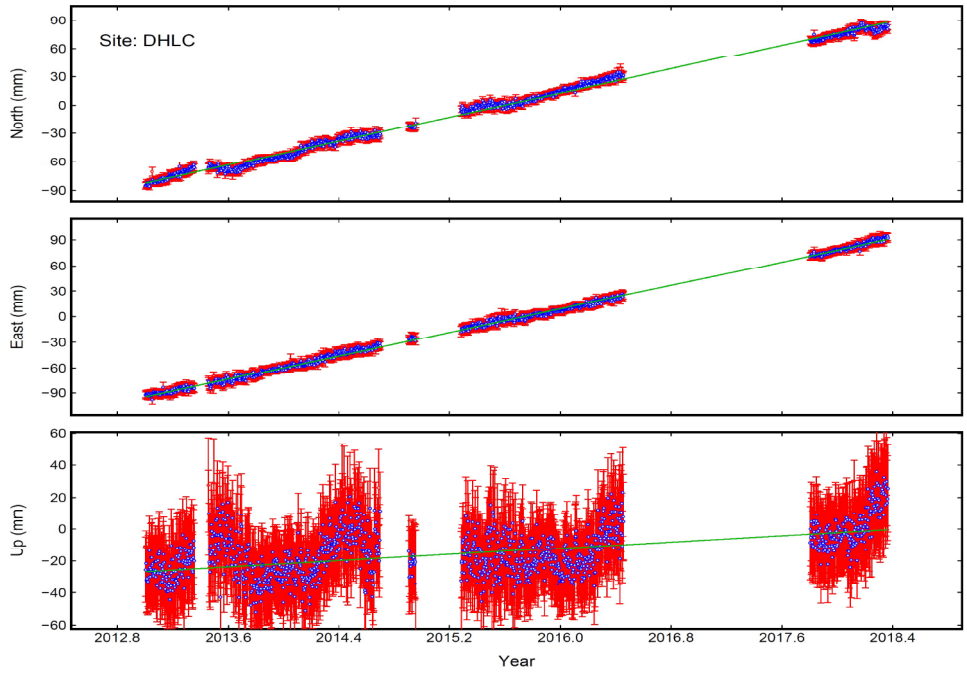

Fig. 3.13: Time series plot of DHLC station.

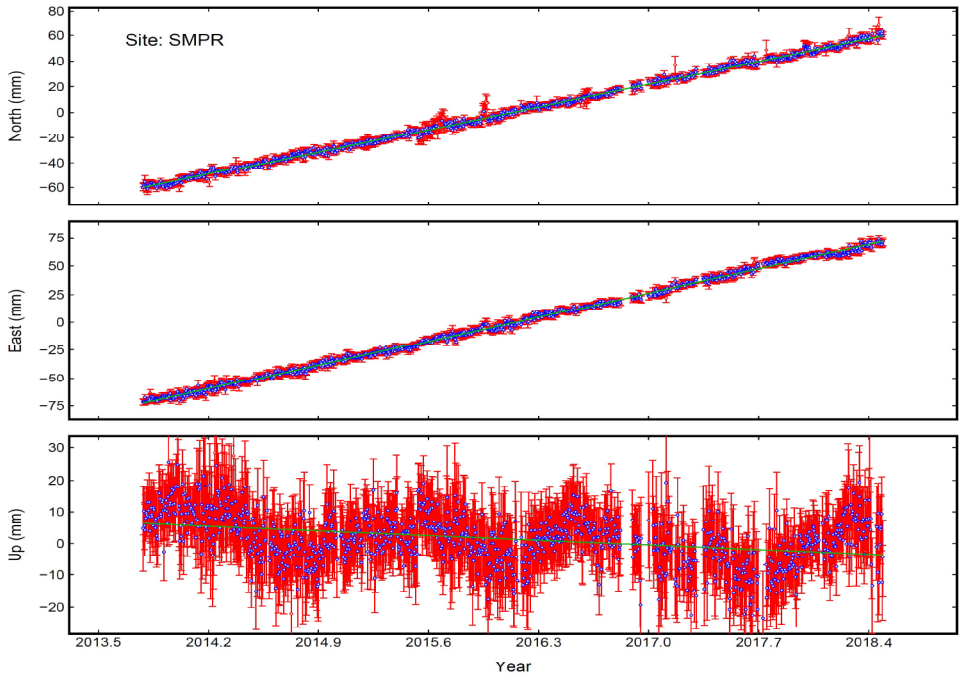

Fig. 3.14: Time series plot of SMPR station.

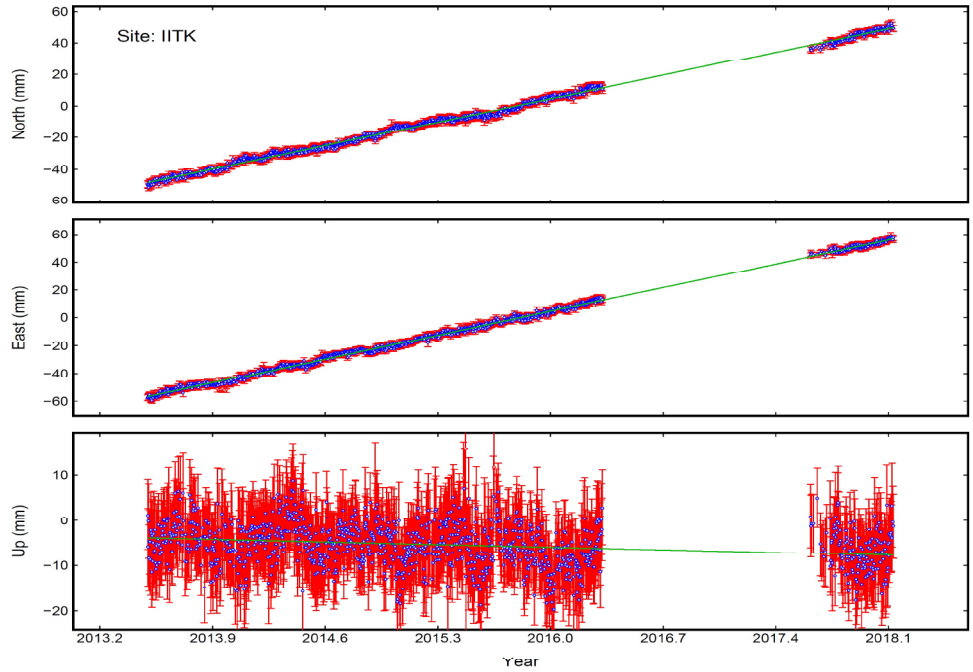

Fig. 3.15: Time series plot of IITK station.

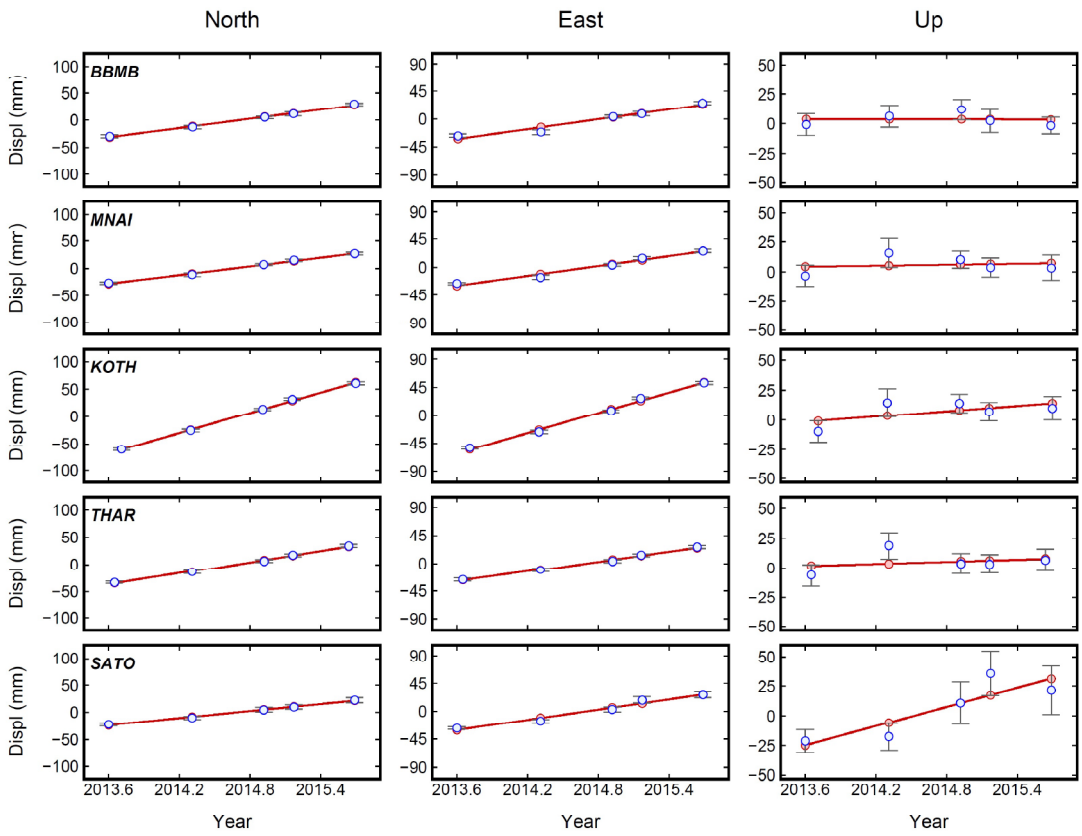

Fig. 3.16: Time series plot of campaign stations in transect T1.

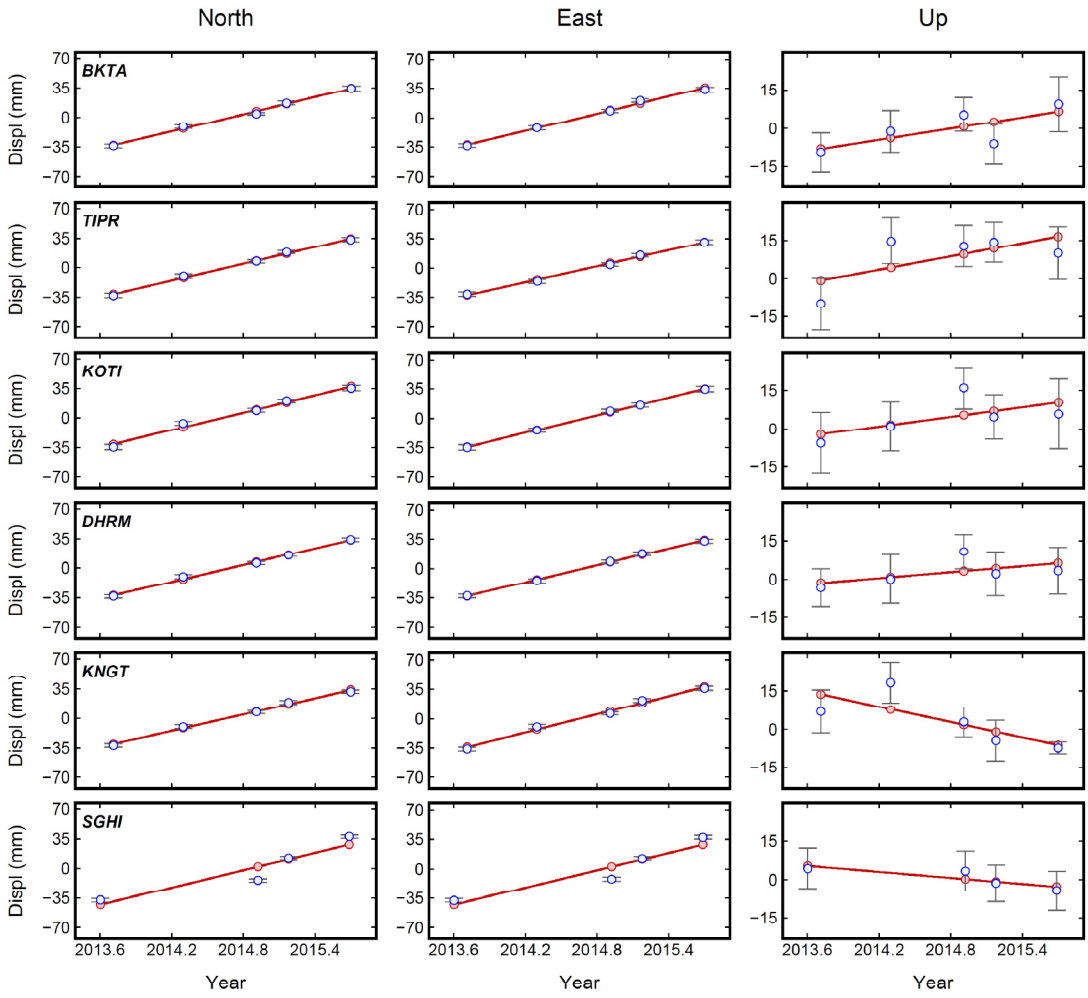

Fig. 3.17: Time series plot of campaign stations in transect T2.

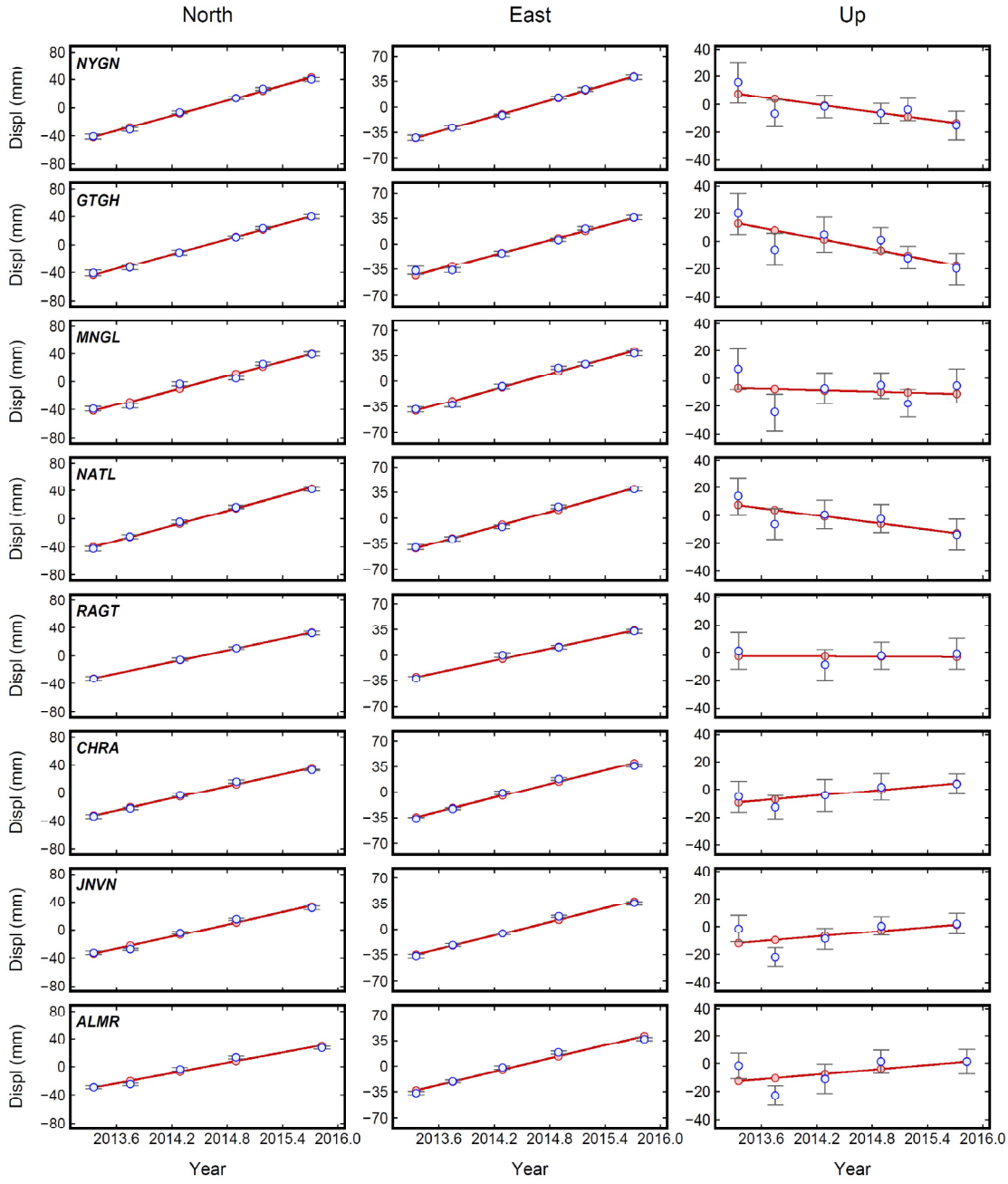

Fig. 3.18: Time series plot of campaign stations in transect T3.

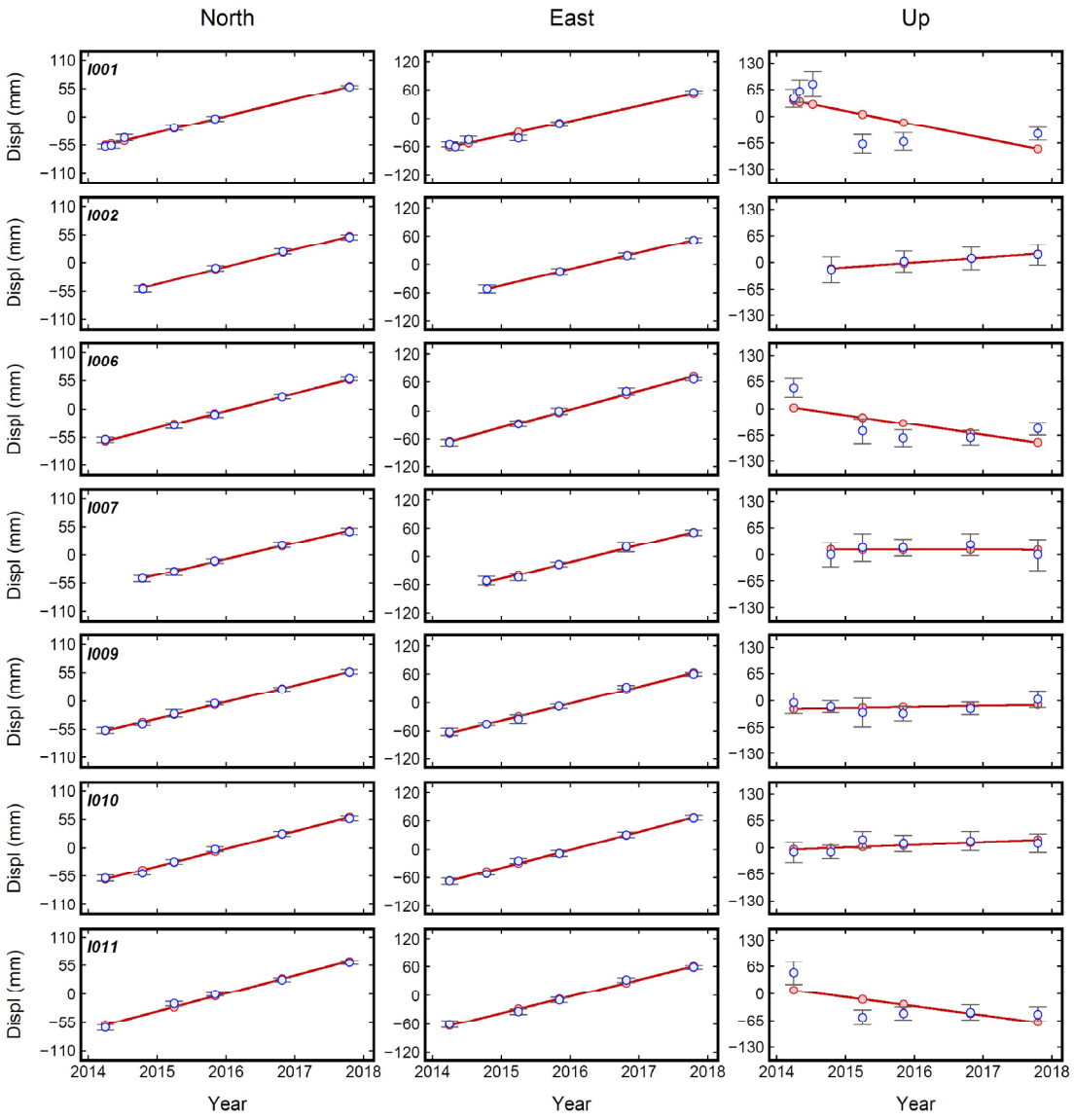
North
East
Up
I001
I002
I006
I007
I009
I010
I011
Displ (mm)
Year
2014
2015
2016
2017
2018

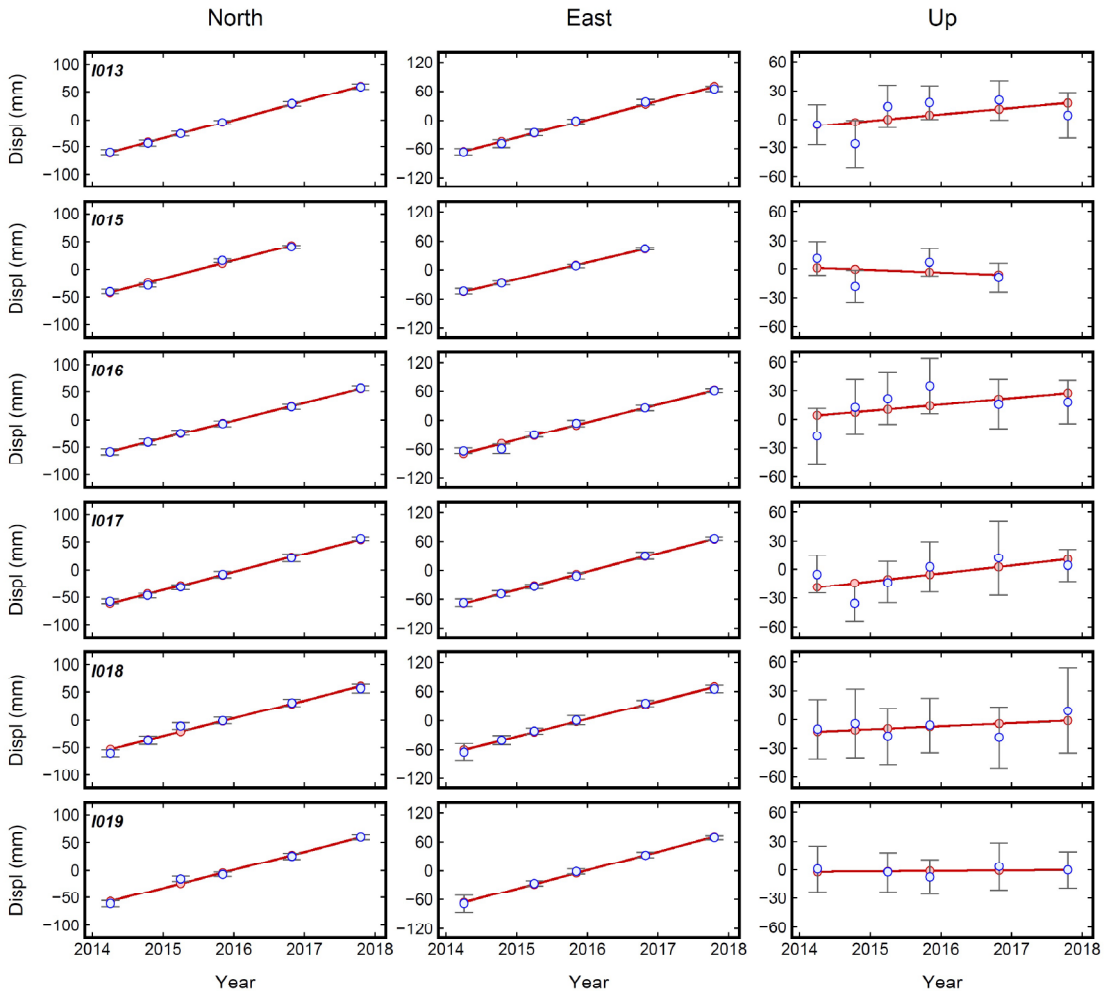

Fig. 3.19: Time series plot of campaign stations in transect T4.

Table 3.5: GPS velocities along transect T1

Site	Longitude (° E)	Latitude (° N)	Component of velocity (mm/yr)	GPS velocities along transect T1	
				ITRF08 reference frame	India-fixed reference frame
MUKE	75.6849	31.9682	North	33.28±0.71	−1.08±0.71
			East	29.95±0.72	−2.08±0.72
			Vertical	−0.12±0.44	−0.12±0.44
BBMB	75.8651	31.9528	North	32.95±1.49	−1.47±1.49
			East	30.95±1.48	−1.15±1.48
			Vertical	−1.52±8.66	−1.52±8.66

MNAI	76.1356	32.1181	North	29.92±1.43	−4.58±1.43
			East	30.13±1.45	−1.94±1.45
			Vertical	4.72±7.05	4.72±7.05
KOTH	76.2003	32.1834	North	32.55±2.10	−1.97±2.10
			East	26.51±2.15	−5.54±2.15
			Vertical	-3.39±7.98	−3.39±7.98
THAR	76.2370	32.2135	North	35.08±2.01	0.55±2.01
			East	30.95±2.01	−1.09±2.01
			Vertical	−5.01±16.78	−5.01±16.78
SATO	76.2922	32.2432	North	24.99±1.99	−9.55±1.99
			East	31.33±1.99	−0.70±1.99
			Vertical	10.82±15.30	10.82±15.30
BRMR	76.5436	32.4397	North	27.46±0.71	−7.15±0.71
			East	25.72±0.79	−6.26±0.79
			Vertical	2.43±0.43	2.43±0.43

Table 3.6: GPS velocities along transect T2

Site	Longitude (° E)	Latitude (° N)	Component of velocity (mm/yr)	GPS velocities along transect T2	
				ITRF08 reference frame	India-fixed reference frame
CHD1	76.7609	30.7674	North	32.11±0.60	−2.57±0.60
			East	31.88±0.70	−1.30±0.70
			Vertical	−11.61±0.25	−11.61±0.25
BKTA	76.9115	30.7394	North	33.75±1.21	−0.97±1.21
			East	32.06±1.23	−1.19±1.23
			Vertical	5.78±5.71	5.78±5.71
TIPR	76.9385	30.8139	North	32.61±1.27	−2.12±1.27
			East	31.31±1.31	−1.90±1.31
			Vertical	17.53±9.17	17.53±9.17
KOTI	76.9879	30.8368	North	33.27±1.58	−1.47±1.58
			East	33.31±1.63	0.10±1.63
			Vertical	11.97±7.90	11.97±7.90
DHRM	77.0244	30.8976	North	33.62±1.11	−1.13±1.11

			East	32.84±1.15	−0.34±1.15
			Vertical	8.91±5.62	8.91±5.62
KNGT	77.1071	30.9692	North	34.39±1.47	−0.38±1.47
			East	34.82±1.47	1.66±1.47
			Vertical	−9.21±5.45	−9.21±5.45
SGHI	77.1309	31.0440	North	34.85±1.57	0.07±1.57
			East	32.31±1.58	−0.8±1.58
			Vertical	−10.13±18.46	−10.13±18.46
THEO	77.3359	31.1231	North	34.82±0.75	−0.02±0.75
			East	30.96±0.77	−2.16±0.77
			Vertical	−10.67±0.67	−10.67±0.67

Table 3.7: GPS velocities along transect T3

Site	Longitude (° E)	Latitude (° N)	Component of velocity (mm/yr)	GPS velocities along transect T3	
				ITRF08 reference frame	India-fixed reference frame
THKD	78.8569	29.1486	North	34.81±0.40	−0.44±0.40
			East	34.94±0.40	0.07±0.40
			Vertical	−3.15±0.16	−3.15±0.16
NYGN	79.3143	29.2743	North	36.23±1.14	0.87±1.14
			East	33.65±1.19	−1.28±1.19
			Vertical	−7.95±5.71	−7.95±5.71
GTGH	79.3768	29.3284	North	36.28±1.54	0.9±1.54
			East	36.01±1.75	1.09±1.75
			Vertical	−11.55±5.99	−11.55±5.99
MNGL	79.3874	29.3466	North	34.24±1.27	−1.14±1.27
			East	32.41±1.31	−2.50±1.31
			Vertical	−3.27±6.67	−3.27±6.67
NATL	79.4425	29.3879	North	34.65±1.33	−0.75±1.33
			East	33.89±1.37	−1.01±1.37
			Vertical	−0.13±8.61	−0.13±8.61
RAGT	79.4809	29.4500	North	33.31±1.71	−2.10±1.71
			East	28.06±1.93	−6.81±1.93

			Vertical	3.65±7.52	3.65±7.52
CHRA	79.4966	29.5004	North	32.55±1.54	−2.86±1.54
			East	35.64±1.44	0.80±1.44
			Vertical	4.84±6.12	4.84±6.12
JNVN	79.5488	29.5465	North	32.75±1.41	−2.67±1.41
			East	35.57±1.45	0.74±1.75
			Vertical	11.62±5.37	11.62±5.37
ALMR	79.6708	29.6152	North	28.85±1.53	−6.61±1.53
			East	35.57±1.61	0.75±1.61
			Vertical	8.42±5.95	8.42±5.95
DHLC	79.7870	29.6741	North	32.01±0.70	−3.47±0.70
			East	33.77±0.80	−1.05±0.80
			Vertical	2.32±0.43	2.32±0.43

Table 3.8: GPS velocities along transect T4

Site	Longitude (° E)	Latitude (° N)	Component of velocity (mm/yr)	GPS velocities along transect T4	
				ITRF08 reference frame	India-fixed reference frame
I001	79.4110	29.3683	North	31.88±1.21	−3.51±1.21
			East	32.40±1.14	−2.50±1.14
			Vertical	−15.93±5.48	−15.93±5.48
I002	79.3183	29.4082	North	33.74±2.51	−1.63±2.51
			East	33.66±2.79	−1.19±2.79
			Vertical	5.88±12.58	5.88±12.58
I006	79.3187	29.3525	North	32.70±1.53	−2.67±1.53
			East	36.24±1.75	1.36±1.75
			Vertical	−16.30±6.95	−16.30±6.95
I007	79.3192	29.3739	North	30.18±2.53	−5.19±2.53
			East	34.72±2.92	−0.15±2.92
			Vertical	−1.87±13.24	−1.87±13.24
I009	79.2684	29.3753	North	31.95±1.41	−3.40±1.41
			East	35.61±1.52	0.76±1.52
			Vertical	−2.98±6.47	−2.98±6.47

I010	79.2319	29.3571	North	34.06±1.59	−1.28±1.59
			East	37.33±1.74	2.48±1.74
			Vertical	3.41±7.29	3.41±7.29
I011	79.1871	29.3048	North	32.53±1.46	−2.8±1.46
			East	33.98±1.62	−0.89±1.62
			Vertical	−8.86±6.58	−8.86±6.58
I013	79.2429	29.2988	North	32.98±1.62	−2.37±1.62
			East	36.71±1.91	1.82±1.91
			Vertical	1.84±7.65	1.84±7.65
I015	79.3368	29.2952	North	31.00±1.51	−4.37±1.51
			East	33.20±1.65	−1.73±1.65
			Vertical	−5.84±6.72	−5.84±6.72
I016	79.4464	29.3359	North	31.32±1.59	−4.08±1.59
			East	34.79±1.76	−0.14±1.76
			Vertical	2.54±8.49	2.54±8.49
I017	79.5231	29.2308	North	32.88±1.36	−2.86±1.36
			East	37.15±1.61	−3.39±1.61
			Vertical	6.08±6.30	6.08±6.30
I018	79.5539	29.3529	North	31.72±2.32	−4.04±2.32
			East	34.83±2.92	−1.13±2.92
			Vertical	−2.75±12.28	−2.75±12.28
I019	79.5519	29.4369	North	31.76±1.76	−3.67±1.76
			East	36.98±2.20	2.08±2.20
			Vertical	−2.00±7.75	−2.00±7.75

The surface velocity (ITRF08) in all four transects shows northeast directed trend of the Indian plate. The GPS stations in T1 move with the velocity ranging from 37.62±0.14 mm/yr to 46.78±2.84 mm/yr (Fig. 3.20). In transect T2, a higher range of GPS velocities (45.21±1.82 mm/yr to 48.94±2.08 mm/yr) than the transect T1 is observed (Fig. 3.20). Similarly, in transect T3 (43.55±2.58 mm/yr to 51.12±2.33 mm/yr) and T4 (45.42±2.24 mm/yr to 50.53±2.36 mm/yr), observed GPS velocities are higher than that of T1 and T2 (Fig. 3.20). Overall, from west to east, a gradual increase in the velocity pattern along the northwest Himalaya is observed (Fig. 3.20). The vertical velocity along the northwest

Himalaya shows subsidence along the IGP and upliftment along the Lesser Himalaya (Fig. 3.22).

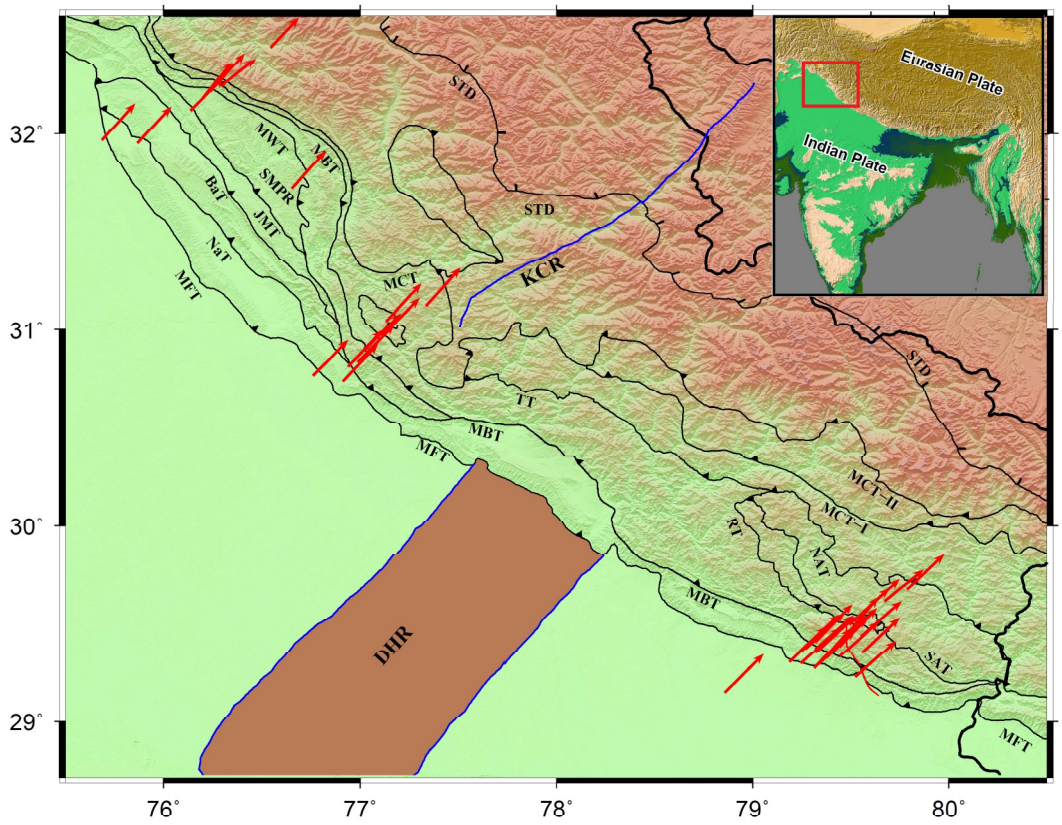

Fig. 3.20: Surface velocities of GPS stations along the northwest Himalaya in the ITRF08 reference frame. Abbreviations are as follows: BaT, Barsar Thrust; DHR, Delhi-Haridwar Ridge; JMT, Jawalamukhi Thrust; KCR, Kaurik Chango Rift; MBT, Main Boundary Thrust; MCT, Main Central Thrust; MFT, Main Frontal Thrust; MWT, Medilicott- Wadia Thrust; NaT, Nalagarh Thrust; NAT, North Almora Thrust; RT, Ramgarh Thrust; SAT, South Almora Thrust; STD, South Tibetan Detachment; TT, Tons Thrust.

Table 3.9: GPS velocities of IGS stations in the ITRF08 reference frame

Site	Longitude (° E)	Latitude (° N)	V_n (mm/yr)	V_e (mm/yr)	V_u (mm/yr)
CHUM	75.7511	42.9985	2.53 ± 0.05	27.46 ± 0.05	−1.38± 0.17
COCO	96.8339	−12.1883	55.28 ± 0.05	42.32± 0.05	0.51± 0.17
DGAR	72.3702	−7.2697	34.23± 0.06	46.14 ±0.08	−0.6 ± 0.26

DRAG	35.3921	31.5932	20.78±0.04	23.51 ±0.04	3.86 ± 0.15
GUAO	87.1773	43.4711	5.01±0.09	31.08 ± 0.08	−1.41 ± 0.3
HYDE	78.5509	17.4173	37.41 ±0.04	40.19 ± 0.04	1.52 ± 0.14
IISC	77.5704	13.0212	36.03±0.04	42.16± 0.05	−2.37 ± 0.17
KIT3	66.8855	39.1348	4.52 ± 0.04	27.24 ± 0.04	−0.43 ± 0.16
KRTV	78.6191	50.7139	0.73 ±0.04	26.49± 0.04	−1.13± 0.15
LCK2	80.9559	26.9126	34.05±0.19	35.64± 0.21	−1.73 ±0.77
LHAZ	91.104	29.6573	15.72 ± 0.04	44.91± 0.04	−2.33 ± 0.15
POL2	74.6943	42.6798	4.71± 0.03	26.89 ± 0.03	−2.26 ± 0.12
SOLA	46.4006	24.9107	28.96 ±0.10	30.12± 0.10	−4.21 ± 0.38
TEHN	51.3341	35.6973	21.60± 0.05	23.81±0.05	−6.47 ± 0.16
URUM	87.6007	43.8079	1.07 ± 0.04	29.5 ±0.04	0.47 ± 0.13
WUHN	114.3573	30.5317	−11.86±0.08	32.86± 0.08	−0.41±0.33

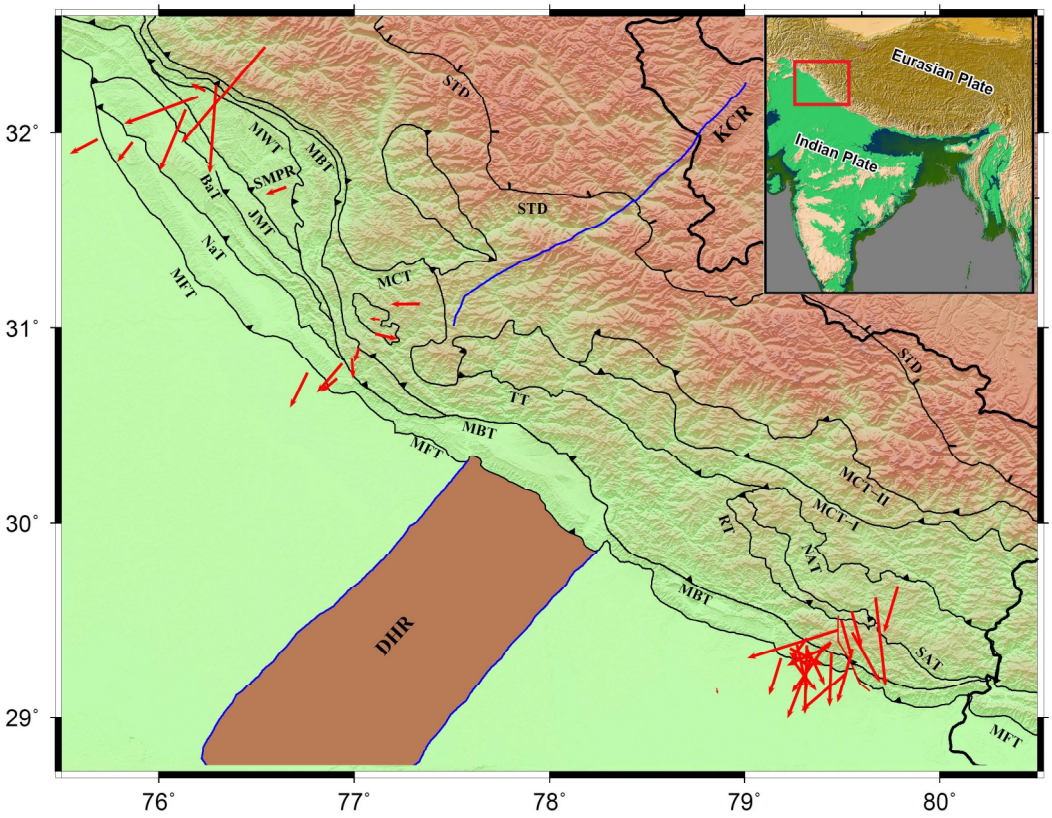

Fig. 3.21: Surface velocities of GPS stations along the northwest Himalaya in the India-fixed reference frame. Abbreviations are same as Fig. 3.20.

To increase the spatial resolution of the surface velocity field, an updated set of 446 published horizontal velocities covering the whole Himalayan arc is incorporated. These surface velocities [e.g., 21, 86, 88, 154, 158, 187, 221, 323] were combined with regional velocities in the ITRF08 reference frame using a seven parameter Helmert transformation (Equation 3.16).

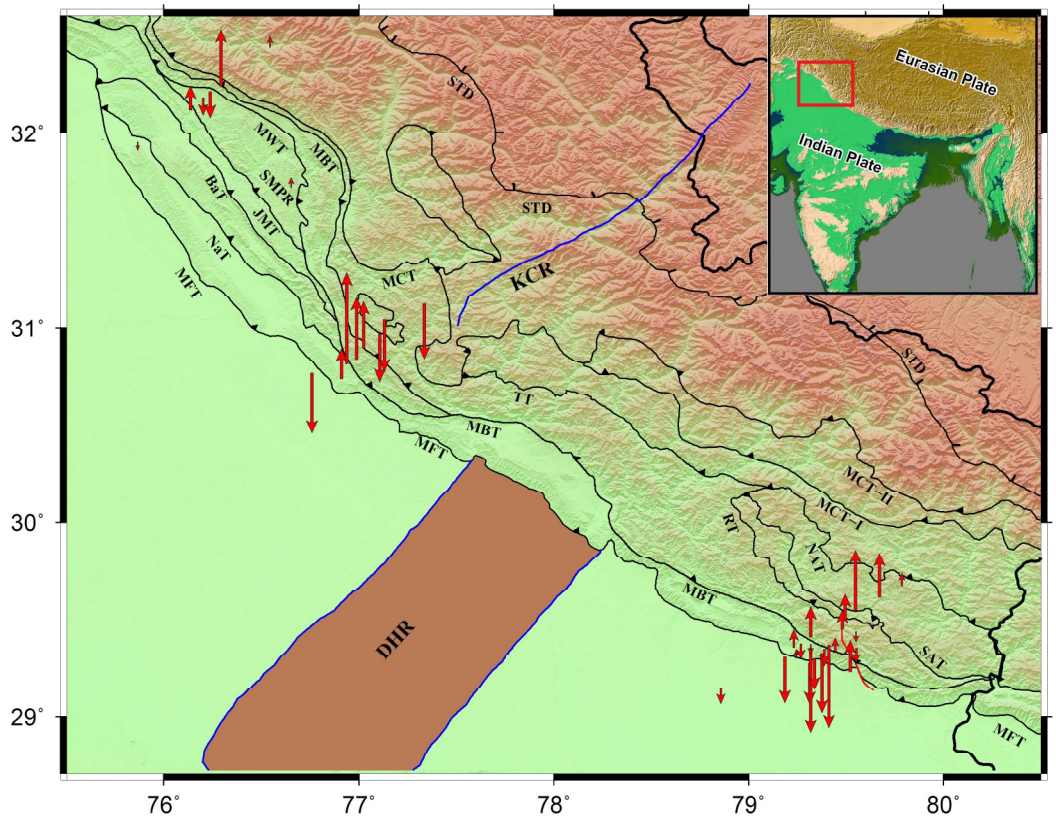

Fig. 3.22: Vertical velocities of GPS stations along northwest Himalaya. Abbreviations are same as Fig. 3.20

$$\begin{bmatrix} X \\ Y \\ Z \end{bmatrix}_{(dataset2)} = \begin{bmatrix} X \\ Y \\ Z \end{bmatrix}_{(dataset1)} + \begin{bmatrix} T_X \\ T_Y \\ T_Z \end{bmatrix} + \begin{bmatrix} 0 & -R_Z & R_Y \\ R_Z & 0 & -R_X \\ -R_Y & R_X & 0 \end{bmatrix} \begin{bmatrix} X \\ Y \\ Z \end{bmatrix}_{(dataset1)} + D \begin{bmatrix} X \\ Y \\ Z \end{bmatrix}_{(dataset1)} \tag{3.16}$$

The process of combining two datasets is performed by rotating one dataset of velocities with respect to the other through the estimation of a seven-parameter Helmert transformation in order to ensure the alignment of both datasets into a common reference frame

[154]. To combine the published velocities with the regional velocities of the four transects, a three step process is followed.

Step I: The observed data from regional network are processed using GAMIT-GLOBK software in the ITRF00, ITRF05, and ITRF08 reference frame.

Step II: A seven-parameter Helmert transformation (Equation 3.16) is utilized to convert the observed data from one reference frame to another reference frame (e.g., ITRF05 to ITRF08).

Step III: Then, the velocity residuals of co-located stations in both datasets are minimized in a least-squares sense. Thereafter, these best-fitted transformation parameters are used to convert all other published velocities into the ITRF08 reference frame.

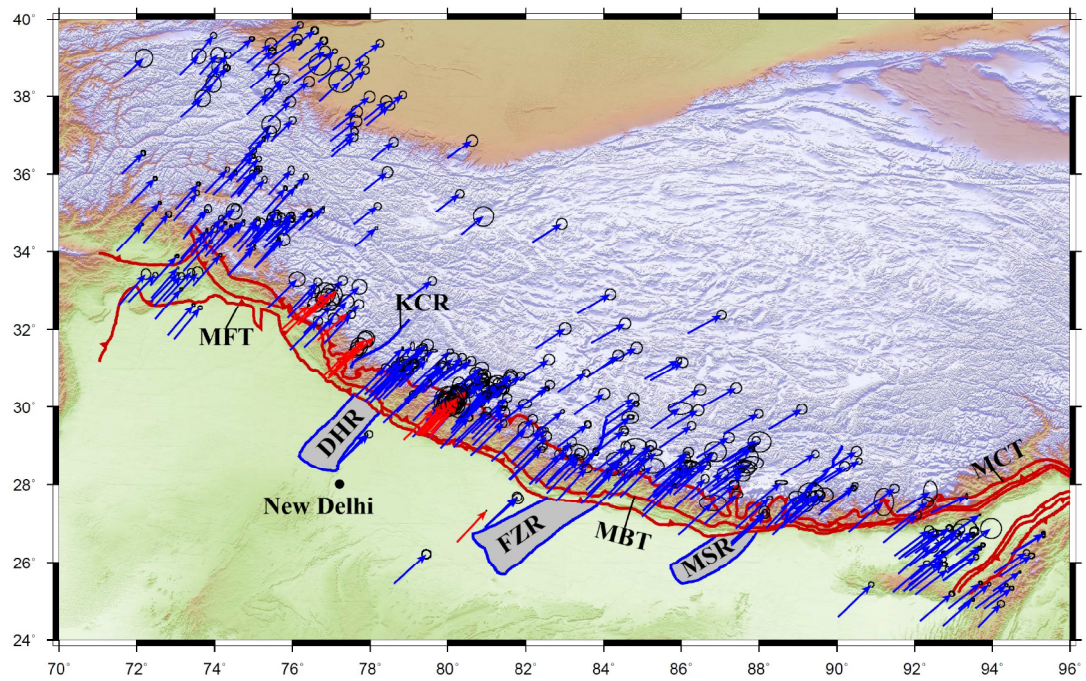

Fig. 3.23: Surface velocity field in the ITRF08 reference frame along the Himalayan arc. Red arrows represent horizontal velocities obtained from 41 new regional GPS stations, whereas the blue arrows indicate surface velocities acquired from published results. Abbreviations are as follows: DHR, Delhi-Haridwar Ridge; FZR, Faizabad Ridge; MBT, Main Boundary Thrust; MCT, Main Central Thrust; MFT, Main Frontal Thrust; MSR, Munger-Saharsa Ridge;

The final horizontal velocity field (ITRF08 reference frame) comprising 486 GPS

stations lies in the range of 37−56 mm/yr, with uncertainties lying in the range of 2−3 mm/yr (Fig. 3.23). Additionally, the velocity field in the India-fixed reference frame (Fig. 3.24) is also obtained to account for the regional deformation pattern using the Euler pole of Jade et al. (2017) [116].

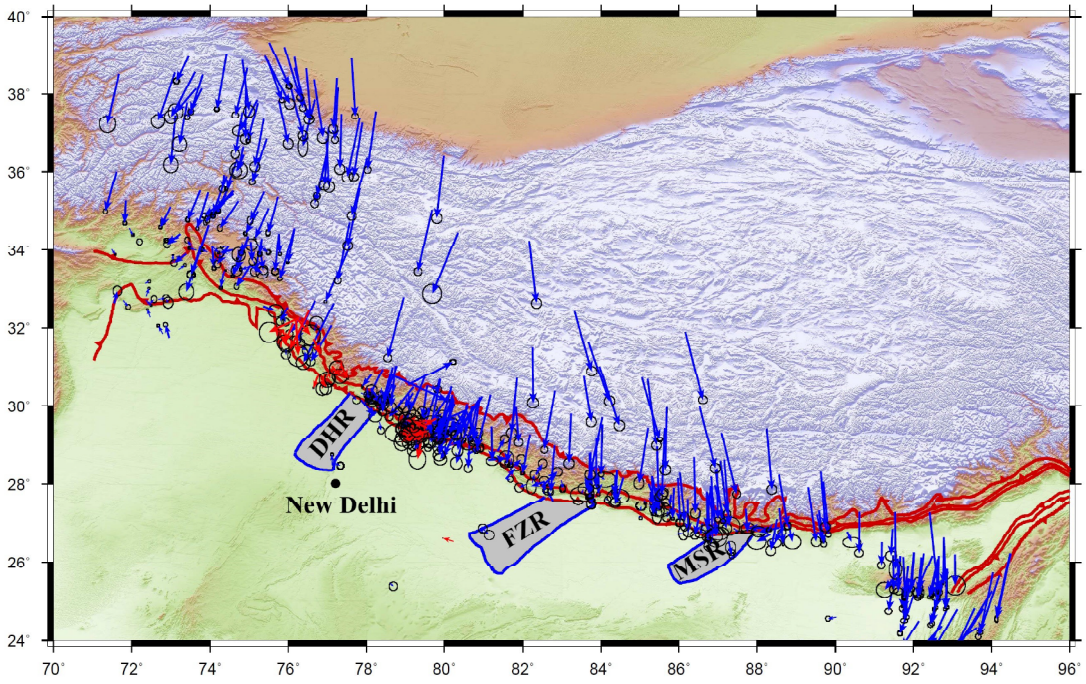

Fig. 3.24: Surface velocity field in the India-fixed reference frame along the Himalayan arc. Red arrows represent horizontal velocities obtained from 41 new regional GPS stations, whereas the blue arrows indicate surface velocities acquired from published results. Abbreviations are same as Fig. 3.23.

3.6 Strain rate field along the Himalayan arc

As crustal strain describes geological and tectonic changes during the deformation, knowledge of its distribution and amplitude is of huge importance for a better understanding of the ongoing tectonic activity. The displacement $u_i(x)$ at any arbitrary point x with respect to the origin x_0 can be expanded in terms of a Taylor series expansion as below:

$$u_i(x) = u_i(x_0) + \frac{1}{2}\left(\frac{\partial u_i}{\partial x_j} + \frac{\partial u_j}{\partial x_i}\right) dx_j + \frac{1}{2}\left(\frac{\partial u_i}{\partial x_j} - \frac{\partial u_j}{\partial x_i}\right) dx_j \ldots i = 1,2,3 \qquad (3.17)$$

Here, $u_i(x_0)$ indicates a rigid body translation and the subsequent partial derivatives represent relative displacement in terms of the gradient of displacement. The symmetric part of the displacement gradient tensor is defined as an infinitesimal small strain tensor in the following manner.

$$\varepsilon_{ij} = \frac{1}{2}\left(\frac{\partial u_i}{\partial x_j} + \frac{\partial u_j}{\partial x_i}\right) \tag{3.18}$$

The anti-symmetric part of the displacement gradient tensor can be represented as a rigid body rotation as:

$$\omega_{ij} = \frac{1}{2}\left(\frac{\partial u_i}{\partial x_j} - \frac{\partial u_j}{\partial x_i}\right) \tag{3.19}$$

Thus, the surface displacement has three major components: rigid body translation $(u_i(x_0))$, strain (ε_{ij}), and rigid body rotation (ω_{ij}). Further, a 2D strain rate field can be formed from Equation (3.17) as

$$\dot{\varepsilon}_{1,2} = \frac{\dot{\varepsilon}_{ee} + \dot{\varepsilon}_{nn}}{2} \pm \sqrt{\frac{1}{4}(\dot{\varepsilon}_{ee} + \dot{\varepsilon}_{nn})^2 + \dot{\varepsilon}_{en}^2} \tag{3.20}$$

$$\theta = \frac{1}{2} tan^{-1}\left(\frac{2\dot{\varepsilon}_{en}}{\dot{\varepsilon}_{ee} - \dot{\varepsilon}_{nn}}\right) \tag{3.21}$$

$$\dot{\varepsilon} = \sqrt{\dot{\varepsilon}_{ee}^2 + \dot{\varepsilon}_{nn}^2 + 2\dot{\varepsilon}_{en}^2} \tag{3.22}$$

where, $\dot{\varepsilon}_1$ and $\dot{\varepsilon}_2$ are principal axes of strain; $\dot{\varepsilon}_{ee} = \frac{\partial v_e}{\partial x_e}$, $\dot{\varepsilon}_{nn} = \frac{\partial v_n}{\partial x_n}$, $\dot{\varepsilon}_{en} = \frac{1}{2}\left(\frac{\partial v_e}{\partial x_e} + \frac{\partial v_n}{\partial x_n}\right)$; and v_e and v_n are the east and north velocity components, respectively [287]. In the right hand side of Equation (3.20), the first term represents dilatation strain rate and the second term indicates maximum shear strain rate; θ in Equation (3.21) shows the directional principal strain rate. The second invariant strain rate $(\dot{\varepsilon})$ is represented by Equation (3.22).

Several methods, such as the grid method, subnetwork method, and the Delaunay triangulation technique exist for the estimation of the strain rate by solving the velocity gradient tensor [5, 55, 96, 135, 266].

In the present study, the whole Himalayan arc is divided into uniform grids ($0.25^\circ \times 0.25^\circ$). The derived horizontal velocities are used for estimation of the two-dimensional velocity gradient tensor that models strain rate as a continuous function [266].

$$W_i = \exp\left(\frac{-d_1^2}{2D^2}\right) \tag{3.23}$$

Here, W_i is the weighting factor; d_i is the distance between the i^{th} GPS site and the i^{th} node point, and D is the space of the fourth closest station in a grid to the estimating point. The factor D controls smoothing of the geodetic strain rate field. The choice of D depends both on the spacing of the GPS network and the scale of the problem of interest [55, 266]. Thus, the value of D varies from region to region and network to network [5, 55]. To account for the variation in the strain rate due to the smoothing parameter, it is varied from 80 km to 120 km. The results are summarized in Table 3.10.

Table 3.10: Variation in strain rate due to changes in the smoothing parameter value

Smoothing parameter (D)	Min($\dot{\varepsilon}_1$) (10^{-8} strain/yr)	Max($\dot{\varepsilon}_1$) (10^{-8} strain/yr)	Min($\dot{\varepsilon}_2$) (10^{-8} strain/yr)	Max($\dot{\varepsilon}_2$) (10^{-8} strain/yr)	GPS vector usage (%)
80 km	−5.68	24.5	−29.4	6.58	71
100 km	−5.3	29.8	−22.6	6.22	82
120 km	−4.35	23.5	−38.8	5.51	84

It may be noted that the present work concentrates on finding the maximum strain variation (i.e., the first order strain anomalies) rather than finding the highly localized strain gradients (i.e., the localized strain due to regional structures) [5, 170]. From Table 3.10, it is observed that the maximum strain rate variation (i.e., $\dot{\varepsilon}_1$ and $\dot{\varepsilon}_2$) corresponds to D =100 km with 82% GPS vector usage in the strain rate calculation. Therefore, the smoothness radius is considered as 100 km which also corresponds to the maximum strain rate variation in the study area. The calculation of 2D strain rate and rotation rate provides a picture of ongoing crustal deformation activities and geodynamic processes such as the fault strain accumulation [55]. Note that the strain and rotation rate tensors are independent of any reference frame [55]. The principal axes of strain rate ($\dot{\varepsilon}_1$ and $\dot{\varepsilon}_2$) show the nature and direction of the deformation. For instance, when an eigenvalue is negative, it represents shortening (compression) [55], whereas a positive eigenvalue represents lengthening (extension) [55]. In order to investigate the nature of the deformation pattern, the dilatation, maximum shear, and rotation strain rates are discussed below.

3.6.1 Dilatation strain rate

The dilatation strain rate is the first order invariant of strain rate tensor because it is independent of the coordinate reference frame. It shows the change in the area and is

represented by the sum of eigenvalues of strain rate tensor. Dilatation strain rate is used to discriminate the deformation associated with reverse or thrust faults from the deformation related to normal faults [55].

Fig. 3.25 depicts dilatation strain rate pattern along the whole Himalayan arc; the negative values indicate compression and positive values represent extension. It is observed that the compressional strain rates (-150 nstrain/yr to -200 nstrain/yr) are more dominant than the extensional strain rates ($\sim$80 nstrain/yr to $\sim$90 nstrain/yr), probably due to the presence of the recognized thrust faults. However, some patches of the extension are also noticeable along the Hindu-Kush, Pamir, and the Tibetan Plateau (Fig. 3.25). The main reason for the extension at about 72°E, 38°N (that pertains to the Pamir region of NW Himalaya) is due to the normal faulting in this region [e.g., 13, 42, 52, 236, 279]. This observation agrees to Ischuk et al. (2013) [109] who have carried out extensive study on this region using GPS geodesy (Fig. 3.25). Their findings clearly suggest the evidence of extension and negligible shortening in these areas [109].

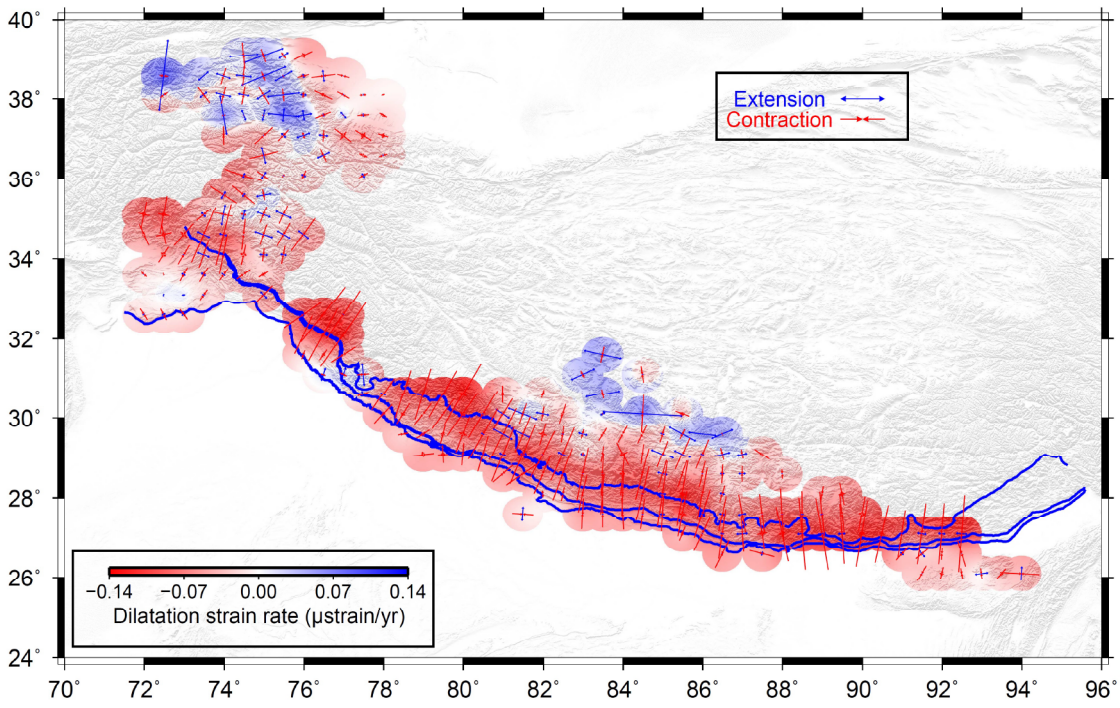

Fig. 3.25: Principal axes of strain rates along the Himalayan arc. Abbreviations are as follows: MBT, Main Boundary Thrust; MCT, Main Central Thrust; MFT, Main Frontal Thrust.

Further, the rapid change from extension to contraction at about 76°E, 38°N is due to

the thrust tectonism in this region, as opposed to the normal faulting in its neighboring region (Fig. 3.25) [13, 42, 52, 109, 198, 236, 279, 324]. The large extension along the region around 85°E, 30°N is because of the lengthening of the Tibetan Plateau in the east-west direction due to some recognized normal faulting (Fig. 3.25) [5, 50, 285]. Apart from this, unusual extension along the eastern Himachal region (around 77°E, 31°N), where MCT bears a lobe shape, is probably due to the prolongation of the DHR beneath the outer Himalaya (Fig. 3.25). Overall, the whole arc is experiencing shortening along the central seismic gap (Fig. 3.25).

3.6.2 Maximum shear strain rate

The maximum shear strain rates reveal the deformation associated with strike-slip faulting. Large values of the maximum shear strain rates indicate a localized shear deformation. These rates are computed through the linear combination of the maximum and the minimum eigenvalues [55].

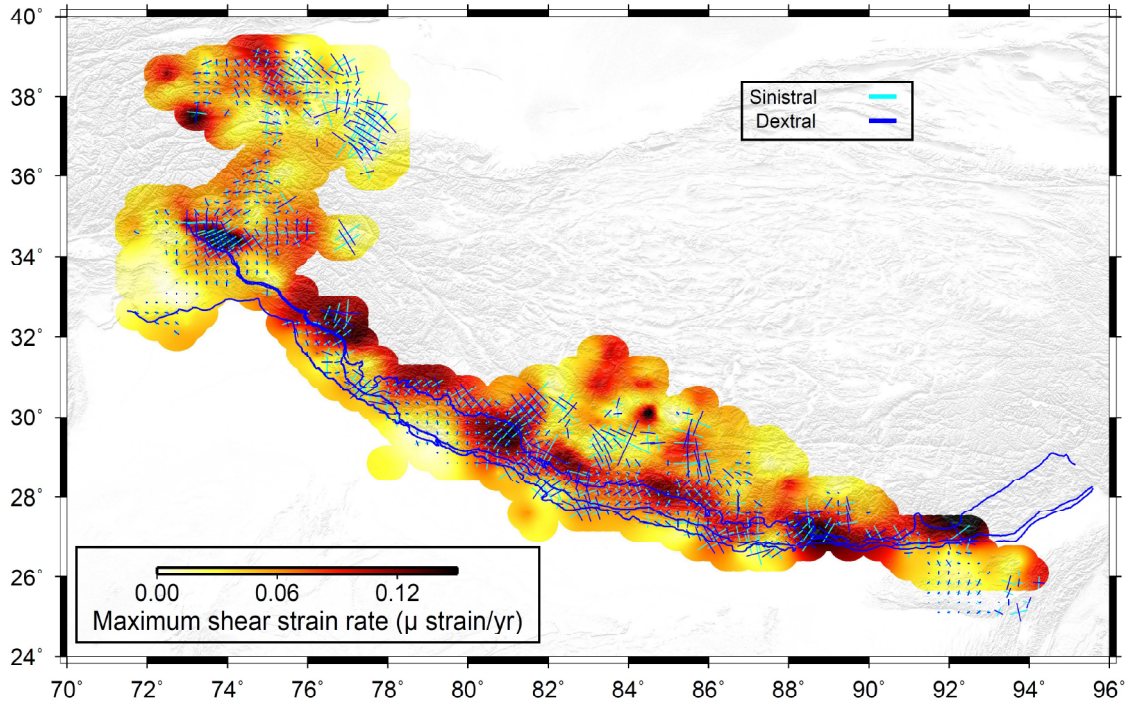

Fig. 3.26: Maximum shear strain rates along the Himalayan arc. Abbreviations are same as Fig. 3.25.

The maximum shear strain rate of about ∼185 nstrain/yr is observed in some areas north of MCT (in the central and northeast Himalaya). This confirms the presence of major strike-slip faults in this region (Fig. 3.26). Larger shear strain rates in the north of the MCT between 75°E and 80°E are probably produced by the strike-slip Karakorum fault and the NW−SE extending KCR (Fig. 3.26) [20, 62, 143]. Another patch of large maximum shear strain rates is noticed along the Bhutan Himalaya, where the creeping activity is controlled by the YDR, Assam block and the Shillong Plateau [299]. Apart from this, no significant evidence of large shear deformation is observed along the Himalayan arc.

3.6.3 Rotation rate

The rotation rate is a representative of the antisymmetric part of the velocity gradient tensor (Equation (3.17)). There are three postulates related to the cause of rotational strain. These are: (i) non-uniform distribution of gravitational potential energy, (ii) heat flux variation of lithosphere, and (iii) plate boundary interactions and the associated configuration [77, 98, 233]. The third hypothesis of plate boundary interaction suits the tectonic environment of the Himalayan arc, as the Arabian plate and the Hindu Kush Pamir range in the northwest cause counterclockwise rotation and the Sunda block in the northeast causes clockwise rotation of the Himalayan arc [116, 134].

GPS observations along the Himalayan arc suggest that the Indian plate is moving in the northeast direction, which is also reflected in the general pattern of rotation of the Himalayan arc in the clockwise direction [114, 116, 302, 323]. Large clockwise as well as anti-clockwise rotation rates along the central Nepal to the southern Tibet are probably due to the east-west extension of the Tibetan Plateau (Fig. 3.27) [285, 310]. In the upper northwest part (along the Pamir range), the anti-clockwise rotation is dominant, though some patches of clockwise rotation are also evident due to the existence of regional normal faults [109]. Small clockwise rotation along the western Kashmir region is probably caused by the Raisi thrust (Fig. 3.27) [134]. A clear change in the rotation pattern along the northwest Himalaya is noticeable. The rotation pattern changes from clockwise in the Kashmir to anti-clockwise in the Kangra reentrant to clockwise in the eastern Himachal to again anti-clockwise (possibly due to Shimla Klippe) along the Dehradun reentrant (due to the impact of DHR) (Fig. 3.27) [143, 284]. Apart from this, a minor counter-clockwise rotation pattern is also observed in Bhutan Himalaya, probably due to the presence of the Shillong Plateau (Fig. 3.27). Nonetheless, these rotation patterns may also be caused by small block motions along the Himalayan arc.

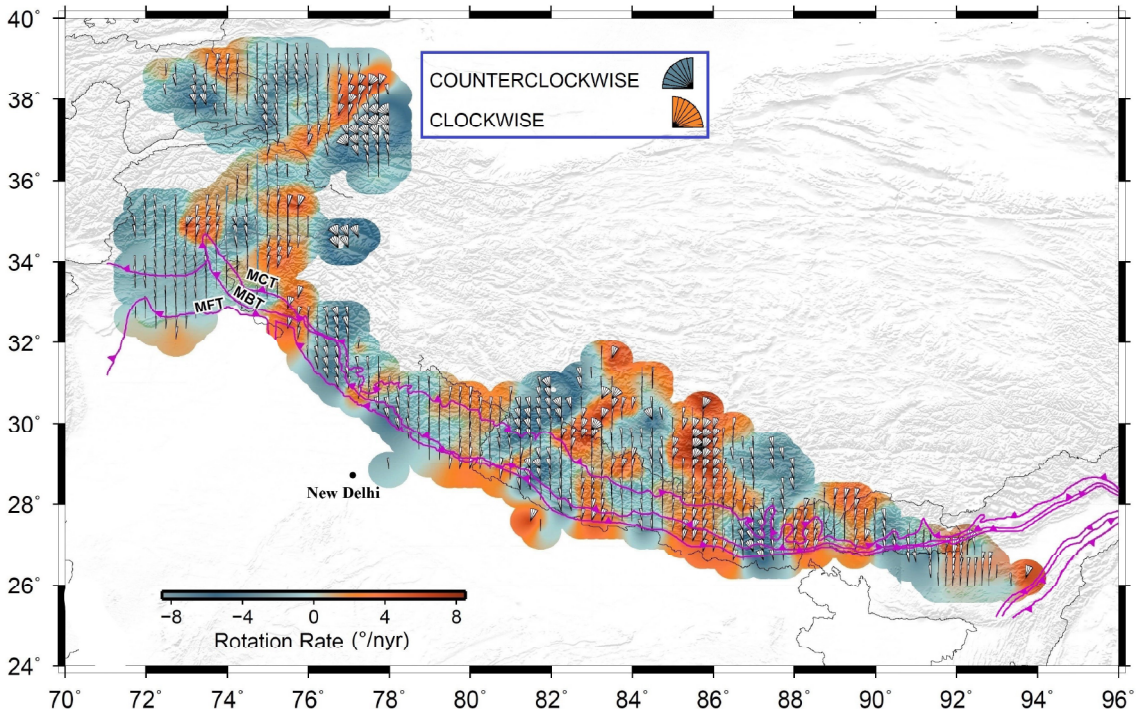

Fig. 3.27: Rotation strain rates along the Himalayan arc. Abbreviations are same as Fig. 3.25.

3.7 Summary

The regional GPS network comprising three arc-normal (T1, T2, and T3) transects and one arc-parallel (T4) transect covers the megathrust system of the Himalaya. This GPS network contains 08 permanent stations and 32 campaign-mode stations. The accrued GPS data from this network were processed utilizing the GAMIT-GLOBK suite of post-processing software. The GPS velocity vectors and daily position time-series plots allowed us to update the horizontal velocity field along the study region. The surface velocity field (ITRF08 frame) in all four transects shows a general northeast directed motion. The horizontal velocities (ITRF08 frame) vary from 37.62±0.14 mm/yr to 50.53±2.36 mm/yr along the four transects. For visualizing the regional deformation along these transects, all surface velocities are rotated to align with an India-fixed reference frame using the rotation pole information given by Jade et al. (2017) [116]. The surface velocities (India-fixed reference frame) vary from 0.45±2.58 mm/yr to 9.50±1.99 mm/yr along these four transects. In addition, the vertical velocities vary from −11.61±0.25 mm/yr to 17.53±9.17 mm/yr along the four transects.

Further, in order to increase the spatial resolution of the surface velocity field along the Himalayan arc, an updated set of 446 published horizontal velocities is incorporated. These surface velocities were combined with the regional velocities in a common reference frame using a seven parameter Helmert transformation. The final surface velocity (ITRF08 frame) field comprising 486 velocity vectors vary between 37 mm/yr and 56 mm/yr with uncertainties lying in the range of 2−3 mm/yr.

Further, the above velocity field is used to calculate the geodetic strain field. It is observed from the dilatation strain rates that the compressional rates (−150 nstrain/yr to −200 nstrain/yr) are more dominant than the extensional rates (80 nstrain/yr to 90 nstrain/yr). From the maximum shear strain rates, it is observed that a region, in the north of the MCT, in the central and the northeast Himalaya is experiencing shear strain (∼185 nstrain/yr), which provides the evidence of the strike-slip faulting in this region. The results from the rotational strain rates suggest that the clockwise rotation in the eastern side and anti-clockwise rotation in the western side of the Tibetan Plateau are probability caused by its east-west extension.

The present chapter has discussed the regional GPS network, data collection, surface velocity field, and the strain rate field along the Himalayan arc. The derived horizontal velocities will be used in Chapter 4 to estimate fault kinematics of the Himalayan megathrust system, whereas the estimated strain rate field will be used in Chapter 5 to calculate geodetic moment rate for the computation of earthquake potential along the Himalayan arc.